Traces of surfactants can severely limit the drag reduction of superhydrophobic surfaces

François J. Peaudecerf[a], Julien R. Landel[b], Raymond E. Goldstein[a], and Paolo Luzzatto-Fegiz[c,1]

[a]Department of Applied Mathematics and Theoretical Physics, Centre for Mathematical Sciences, University of Cambridge, Cambridge CB3 0WA, United Kingdom; [b]School of Mathematics, University of Manchester, Manchester M13 9PL, United Kingdom; and [c]Department of Mechanical Engineering, University of California, Santa Barbara, CA 93106

Edited by William R. Schowalter, Princeton University, Princeton, NJ, and approved May 23, 2017 (received for review February 13, 2017)

Superhydrophobic surfaces (SHSs) have the potential to achieve large drag reduction for internal and external flow applications. However, experiments have shown inconsistent results, with many studies reporting significantly reduced performance. Recently, it has been proposed that surfactants, ubiquitous in flow applications, could be responsible by creating adverse Marangoni stresses. However, testing this hypothesis is challenging. Careful experiments with purified water already show large interfacial stresses and, paradoxically, adding surfactants yields barely measurable drag increases. To test the surfactant hypothesis while controlling surfactant concentrations with precision higher than can be achieved experimentally, we perform simulations inclusive of surfactant kinetics. These reveal that surfactant-induced stresses are significant at extremely low concentrations, potentially yielding a no-slip boundary condition on the air–water interface (the "plastron") for surfactant concentrations below typical environmental values. These stresses decrease as the stream-wise distance between plastron stagnation points increases. We perform microchannel experiments with SHSs consisting of streamwise parallel gratings, which confirm this numerical prediction, while showing near-plastron velocities significantly slower than standard surfactant-free predictions. In addition, we introduce an unsteady test of surfactant effects. When we rapidly remove the driving pressure following a loading phase, a backflow develops at the plastron, which can only be explained by surfactant gradients formed in the loading phase. This demonstrates the significance of surfactants in deteriorating drag reduction and thus the importance of including surfactant stresses in SHS models. Our time-dependent protocol can assess the impact of surfactants in SHS testing and guide future mitigating designs.

superhydrophobic surface | drag reduction | surfactant | Marangoni stress | plastron

Superhydrophobic surfaces (SHSs) combine hydrophobic surface chemistry and micro- or nanoscale patterning to retain a network of air pockets when exposed to a liquid (e.g., reviews in refs. 1–3). Because a large portion of the interface between the solid wall and the liquid is replaced by an air–liquid interface, which can be considered almost as a shear-free surface (known as a "plastron"), SHSs could be used to obtain significant drag reduction in fluid flow applications (4, 5). Microchannel tests have recorded drag reductions of over 20% (e.g., refs. 6–11) and rheometer tests reported slip lengths of up to 185 μm (12). Turbulent flow experiments have reduced drag by up to 75% (13–16). However, a wide range of experiments have provided inconsistent results, with several studies reporting little or no drag reduction (16–25).

A key step toward solving this puzzle has come with the realization that surfactants could induce Marangoni stresses that impair drag reduction. This was first hypothesized to account for experiments that revealed little measurable slip (23, 24), in contradiction with available theoretical predictions based on the absence of surfactants (26–34). Following this hypothesis, surfactants naturally present in water would adsorb onto the air–water interface, as sketched in Fig. 1*A*, and they would be advected by the flow and therefore accumulate at downstream stagnation points, where the interface terminates in a three-phase contact line. The resulting surfactant gradient would then yield a Marangoni stress resisting the fluid motion, thereby decreasing slip and increasing drag (Fig. 1*B*). Traditional models of SHSs are surfactant-free and therefore do not account for this additional drag. This is especially concerning for marine applications, because it is well documented that seawater contains significant amounts of surfactants (35). Rivers, estuaries, and fog also show significant levels of both synthetic and natural surfactants (36, 37).

Recent experiments have shown that whereas a nominally clean flow already displayed slip that was several times below predictions of surfactant-free theories, adding large amounts of surfactant had a barely measurable effect (38). This counterintuitive result appears to undermine the surfactant hypothesis, which would come with the expectation of a strong sensitivity to surfactant concentration. Proving or disproving the surfactant hypothesis, while resolving the above paradox, is essential to design SHSs that can achieve large, reliable drag reduction.

Simulations with Detailed Kinetics

To investigate the flow at extremely low surfactant concentrations, which are essentially impossible to accurately prescribe in experiments, we developed a computational tool for simulating surfactant-laden flows over an SHS whose plane geometry is shown in Fig. 2*A* (full transport model in *SI Model*, *SI Materials and Methods*, and Tables S1 and S2). Neglecting air viscosity, we

Significance

Whereas superhydrophobic surfaces (SHSs) have long promised large drag reductions, experiments have provided inconsistent results, with many textures yielding little or no benefit. Given the vast potential impact of SHSs on energy utilization, finding an explanation and mitigating strategies is crucially important. A recent hypothesis suggests surfactant-induced Marangoni stresses may be to blame. However, paradoxically, adding surfactants has a barely measurable effect, casting doubt on this hypothesis. By performing surfactant-laden simulations and unsteady experiments we demonstrate the impact of surfactants and how extremely low concentrations, unavoidable in practice, can increase drag up to complete immobilization of the air–liquid interface. Our approach can be used to test other SHS textures for sensitivity to surfactant-induced stresses.

Author contributions: F.J.P., J.R.L., R.E.G., and P.L.-F. designed research, performed research, analyzed data, and wrote the paper.

The authors declare no conflict of interest.

This article is a PNAS Direct Submission.

Freely available online through the PNAS open access option.

[1]To whom correspondence should be addressed. Email: fegiz@engineering.ucsb.edu.

This article contains supporting information online at www.pnas.org/lookup/suppl/doi:10.1073/pnas.1702469114/-/DCSupplemental.

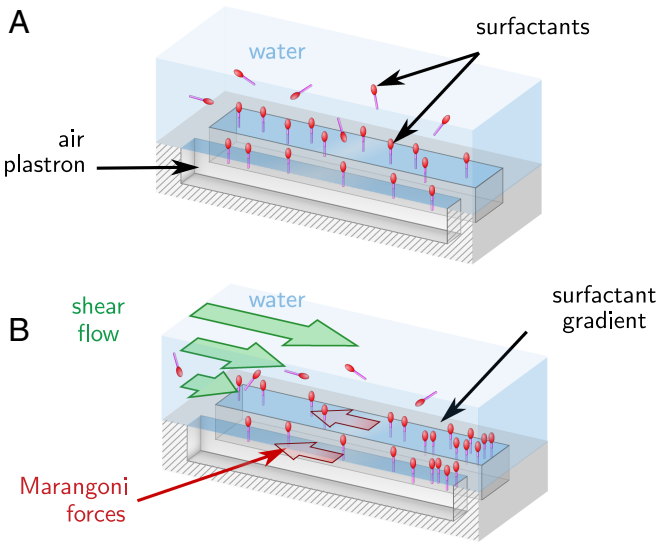

Fig. 1. Presence of surfactants as contaminants can generate Marangoni forces on an SHS. (*A*) Surfactants present in water adsorb at the air–water interface of SHSs. (*B*) In the presence of an external flow, surfactants distribute in gradients between stagnation points. From these gradients Marangoni forces result, resisting the flow and immobilizing the interface.

consider a 2D air–water interface of length g on which surfactants from the bulk can adsorb/desorb and generate Marangoni forces. This interface (in pink in Fig. 2 *A–C*) is on the top of a chamber of depth H and bounded by no-slip ridges of length $\ell/2$ each. The top of the chamber, of length $g+l$, represents a basis element of an SHS. The flow in the chamber is forced by a Poiseuille profile $u(z)$ at $x=0$. In Fig. 2 *B–D*, we show simulation results from very low surfactant concentration to high concentration in the bulk, using the properties of the well-characterized surfactant sodium dodecyl sulfate (SDS) (39). For very low concentration, $c_0=10^{-6}$ mM, the corresponding flow velocity is shown in Fig. 2*B*, with gap length $g=100\,\mu$m, wall length $\ell=50\,\mu$m, channel height $H=100\,\mu$m, and forced Poiseuille flow at $x=0$ of peak speed $50\,\mu\text{m}\cdot\text{s}^{-1}$. The flow field is essentially identical to that for pure water: i.e., $c_0=0$. Fig. 2*D* shows the effect of increasing bulk surfactant concentration on the characteristic drag $\langle\tau\rangle$, which has been spatially averaged over one SHS element of length $g+\ell$. The data, from steady-state simulations with other parameters fixed, are normalized by the corresponding wall shear stress τ_P of the forcing Poiseuille flow. The case $c_0=10^{-6}$ mM, highlighted by the left arrow in Fig. 2*D*, is indeed close to the ideal free-slip drag. The curve in Fig. 2*D* reveals an increase of drag with bulk surfactant concentration, up to the no-slip value, which is reached asymptotically around $c_0=10^{-2}$ mM (right arrow in Fig. 2*D*). The corresponding flow velocity is shown in Fig. 2*C*. A large Marangoni stress appears and the slip velocity is reduced by more than one order of magnitude, practically reaching a no-slip boundary condition at the plastron.

For a bulk concentration of just 10^{-2} mM (that is, 10^{-2} mol·m^{-3}, corresponding to less than 10 g of surfactants per cubic meter of water), the drag flattens to the no-slip asymptote, after which adding more surfactants has little effect. These results explain why adding surfactants in experiments has a barely measurable effect in most cases, because the transition to a regime where Marangoni stresses dominate occurs at extremely small concentrations. Such small concentrations are very difficult to achieve in laboratory experiments, where controlling surfactant contamination [e.g., from SHS manufacturing and materials, water handling, microscopic-particle image velocimetry (μ-PIV) beads, or any surface or fluid, including air, in contact with the water flowing through the microchannel] is exceedingly difficult. Needless to say, such levels of cleanliness are not found in most flow applications. Surfactants at such low concentrations are essentially impossible to detect using a classical tensiometer apparatus, because the corresponding surface tension decrease, in a static fluid, is negligible (39).

The results presented in Fig. 2*D* are generic to other types of surfactants, as shown in Fig. S1. We also note that the properties of the SDS surfactant used in our study do not induce the strongest Marangoni stresses. In fact, its effect is rather mild compared with the surfactants reported in ref. 40. In normal flow applications, we should therefore assume that stronger surfactants than SDS are likely to be present, thus deteriorating even more the performance of the SHS.

The inevitability of surfactants suggests that the main strategy to minimize Marangoni stresses is to optimize the SHS geometry. To test this hypothesis, we simulate flow over 2D basis elements of SHSs with varying interface length g. By increasing the distance g between the upstream and downstream stagnation points, we reduce the average surfactant gradient over the plastron. Fig. 2*E* shows drag vs. interface length for $c_0=10^{-2}$ mM (plotted with red squares). The simulations show that the drag over a contaminated surface is very sensitive to this change of geometry. The drag is also significantly larger than the idealized results for a perfectly clean flow (plotted with red diamonds in Fig. 2*E*) over a large range: $0.01\le g\le 10$ mm.

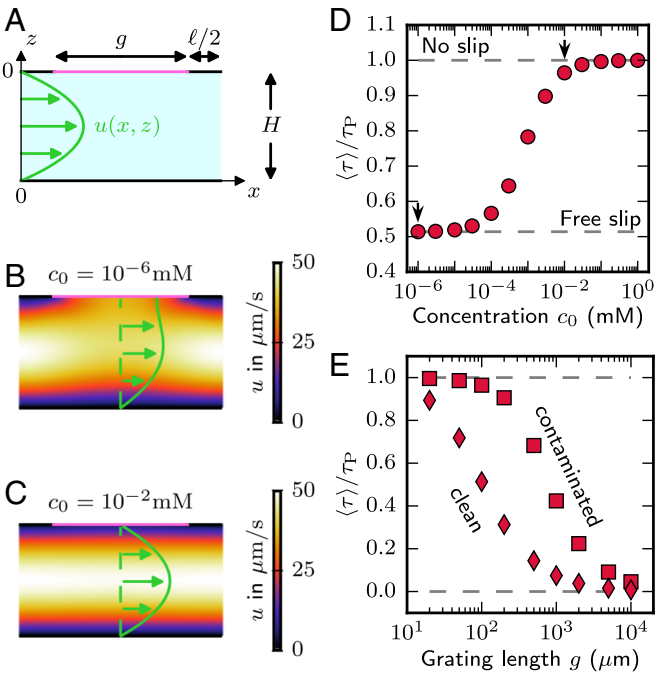

Fig. 2. Numerical simulations of surfactant-laden flows over a 2D SHS. (*A*) Geometry of the simulations for a periodic chamber (i.e., one SHS basis element) of thickness $H=100\,\mu$m with gratings of length $g=100\,\mu$m on the wall at $z=0$, separated with ridges of length $\ell=50\,\mu$m, and with forcing Poiseuille flow at $x=0$. (*B*) Stream-wise velocity u for bulk surfactant concentration $c_0=10^{-6}$ mM, exhibiting slip on the plastron. (*C*) At $c_0=10^{-2}$ mM no slip is reached on the plastron. (*D*) Average normalized drag vs. surfactant concentration. An asymptote is reached at concentrations below those found in the environment. (*E*) Drag vs. grating length, for perfectly clean water (red diamonds) and flow with concentration $c_0=10^{-2}$ mM (red squares), showing that drag reduction in surfactant-laden flows is very sensitive to grating length. All simulations are performed with a peak velocity of the forcing Poiseuille flow of $50\,\mu\text{m}\cdot\text{s}^{-1}$ and fixed ridge length $\ell=50\,\mu$m.

Experiments Show Reduced Slip

To verify the impact of surfactant on plastron slip and the effect of lane length on drag reduction, we performed experiments using μ-PIV on a confocal microscope. We measured the velocity field of gravity-driven microchannel flows in planes parallel to an SHS (Fig. 3 *A–C*, *SI Experimental Protocols*, and Tables S3 and S4). Similar to earlier work (10, 13, 24), our SHSs were made of hydrophobic polydimethylsiloxane (PDMS), using photolithography techniques. The SHSs consisted of stream-wise parallel rectangular lanes or gratings, as shown in Fig. 3*B*. The lane width $w = 40\,\mu$m and ridge width $r = 20\,\mu$m were kept fixed in the experiments. The microchannel height varied slightly, $100 \leq H \leq 130\,\mu$m. We sealed the PDMS chamber using a glass coverslip held in place through Van der Waals adhesion, without surface treatment, to avoid surfactant contamination and to preserve PDMS hydrophobicity. The glass coverslip and chamber were maintained at a fixed temperature within 0.1 °C accuracy through cooling elements. This minimized any potential thermal Marangoni effect (as discussed in *SI Experimental Protocols*) and prevented significant condensation inside the gratings, thus ensuring stability of the plastron over several hours. We used purified water in the experiments and cleaned all possible surfaces in contact with water and microbeads, following a strict cleaning protocol (*SI Experimental Protocols*). The microchannel was connected to inlet and outlet reservoirs whose heights were adjusted separately to enable control of both the background pressure gradient and hydrostatic pressure in the microchannel. The plastron was maintained flat through adjustment of the hydrostatic pressure. The interface position was located with an accuracy of 2 μm.

The symbols in Fig. 3*D* show experimental velocity profiles at several horizontal slices in the case of short lanes, $g = 2\,$mm (SDs in the velocity are indicated with error bars). For comparison, Fig. 3*D* also shows surfactant-free 3D numerical predictions (plotted with solid lines) for the same geometry (*SI Materials and Methods* and Table S5). Similar to theoretical calculations assuming free slip at the plastron, the surfactant-free numerical simulations predict a very large slip, $\max(u/U) \approx 0.8$ at $z_i/H = 1.6\%$ from the plastron (with U the mean flow speed), whereas experimental data at $z/H \leq 2\%$ show no statistically significant slip. A linear extrapolation using the three data values closest to the interface gives a negligible interfacial slip velocity $u_I/U \approx 0.01 \pm 0.02$. In the case of long lanes (Fig. 3*E*), $g = 30\,$mm, experimental data reveal some slip, which is still significantly slower than numerical and theoretical results (26), by ≈85%. A linear extrapolation using the three data values closest to the interface gives $u_I/U \approx 0.14 \pm 0.04$. These results agree with our surfactant-laden simulations reported earlier in Fig. 2*E*: For a given background flow and surfactant concentration, increasing the lane length increases the slip velocity, bringing it closer to predictions from surfactant-free models. This consistency strongly suggests that the reduced slip observed on our experimental SHSs with respect to theoretical predictions comes indeed from traces of unidentified surfactants.

These findings are also consistent with simple scaling analysis. Assuming low interfacial surfactant concentration $\Gamma \ll \Gamma_m$ (with Γ_m the maximum packing concentration) and laminar flow, a force balance at the interface imposes $(1 - u_I/U)/H \sim Ma\langle\Gamma\rangle/(\Gamma_m g)$, with $Ma = 2RT\Gamma_m/(\mu U)$ the Marangoni number, R the gas constant, T the temperature, μ the dynamic viscosity, and $\langle\Gamma\rangle$ the mean concentration over the gap (see *SI Analysis and Discussion of Characteristic Nondimensional Numbers* for details). As Ma ranges from 10^3 to 10^6 in our experiments, this scaling suggests that the no-slip limit, $u_I \ll U$, can be reached for very low surfactant concentrations, as shown by our simulations and suggested by our experiments. The scaling also suggests that an increase in g leads to an increase in u_I, as found in both simulations and experiments. In general $\Gamma(x)$ can have a nonlinear profile (41). As discussed in *SI Analysis and Discussion of*

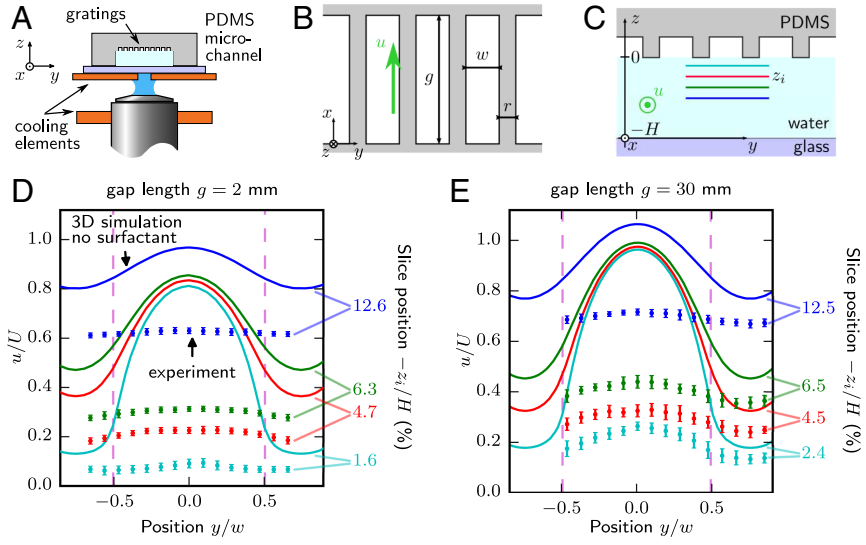

Fig. 3. μ-PIV setup and experimental velocity measurements with constant background flow and comparison with ideal 3D surfactant-free simulations. (*A*) Side view of the inverted PDMS microchannel with a textured SHS on top. The microchannel is in contact with cooling elements and lies above the water objective of the confocal microscope. (*B*) Geometry of the stream-wise parallel rectangular gratings forming the SHS. (*C*) Cross-section at $x = g/2$ of the microchannel. The measuring planes of the μ-PIV at heights z_i are indicated with different colors. (*D*) Lateral distribution of the stream-wise velocity at different heights z_i from the plastron, in the case of short lanes $g = 2\,$mm. The profile is centered on a grating, with the edges of the ridges in dashed magenta lines. Experiments (symbols) show no signicant slip at the plastron, contrary to the strong slip predicted by 3D surfactant-free simulations (lines) for which the velocity is sampled at the same position z_i. (*E*) Same as in *D* in the case of long lanes $g = 30\,$mm. Slip velocity at the plastron is still 85% smaller than predictions from surfactant-free simulations. For *D* and *E*, positions along *z* of the experimental imaging planes and sampling planes in simulations are given in percentage of the total chamber height, with $H = 130\,\mu$m and 100 μm for the chambers in *D* and *E*, respectively. Positions along *y* are normalized by the gap width $w = 40\,\mu$m for both *D* and *E*.

Characteristic Nondimensional Numbers, this does not affect the key findings of this study.

Pressure-Relaxation Experiments for Surfactant Effect

To prove experimentally the surfactant hypothesis while circumventing the difficulty of removing traces of surfactants, we designed time-dependent pressure-relaxation experiments to reveal in situ the presence of surfactant-induced stresses. All of the experiments were conducted with the apparatus shown in Fig. 3 *A–C*, with controlled temperature and interface deflection. These experiments began with a "loading phase," during which the flow was driven by a fixed, strong pressure gradient and allowed to reach steady state (*SI Experimental Protocols* and Tables S6 and S7). The driving pressure was then rapidly decreased to zero while keeping the hydrostatic pressure approximately constant. The change in background pressure gradient was simply achieved by moving the stage onto which the inlet reservoir was attached to the exact level for which both inlet and outlet water levels were at the same vertical position. The motion of the stage was conducted rapidly, within less than 4 s. During the loading phase, which was maintained for 4 min to ensure a steady state was reached, we measured a Poiseuille profile in the microchannel (Fig. S2), giving a mean load speed U (see *SI Experimental Protocols* for details on the technique used to measure U). Our measurements do not reveal significant slip on the SHS side during the loading phase. However, a clear backflow, with negative values (shown in blue in Fig. 4*A*), can be observed after the background pressure gradient vanishes (Movie S1).

Fig. 4*A* shows the time evolution of the lateral profile of the stream-wise velocity measured at $x = g/2$ and $z = -5\,\mu$m for a grating with $g = 30$ mm. The background pressure gradient decreases from a large constant value during the loading phase (mean load speed in the microchannel $U \approx 4.1\,\text{mm}\cdot\text{s}^{-1}$ for $t \leq 5$ s) to zero at $t = 7.2$ s. As the flow is in the Stokes regime ($Re = HU/\nu < 1$, with ν the kinematic viscosity), we expect that, in the absence of surfactants, the velocity should decrease from positive values to zero instantaneously and everywhere as soon as the forcing vanishes. This monotonic behavior can be observed in Fig. 4*A* for the velocity measured above the ridge (green triangles in Fig. 4*B*) and also above wetted gratings (Movie S2). In contrast, the velocity above the plastron (plotted in red and blue in Fig. 4*B* for the middle of the left and right gratings, respectively) decreases sharply to large negative values during the stage motion, corresponding to a flow opposed to the background pressure gradient. This backflow persists for a long time after the background pressure gradient vanishes. In this experiment, it decays over ≈1 min. The same qualitative results and trends are obtained independently of the choice of grating and the direction and intensity of the loading flow, as long as it is sufficiently strong.

During the loading phase, owing to large advection in the flow compared with diffusion and adsorption/desorption kinetics, surfactants at the interface are transported toward the downstream stagnation point of the lane. The concentration of surfactants increases significantly near this point, whereas it decreases everywhere else along the interface. This regime is likely to be analogous to the "stagnant cap regime" described for air bubbles rising in water (41). When the background pressure gradient vanishes, the surfactant-induced stresses are not opposed by viscous stresses any longer, and a Marangoni backflow develops to homogenize the surfactant concentration at the plastron, as shown in Fig. 4*B*. A shear flow establishes across the chamber height, owing to the wall shear stress on the opposite side of the plastron ($z = -H$). As the distribution of surfactant becomes more uniform, surfactant-induced stresses decrease and the backflow diminishes, as shown by the nonlinear temporal trend in Fig. 4*B*.

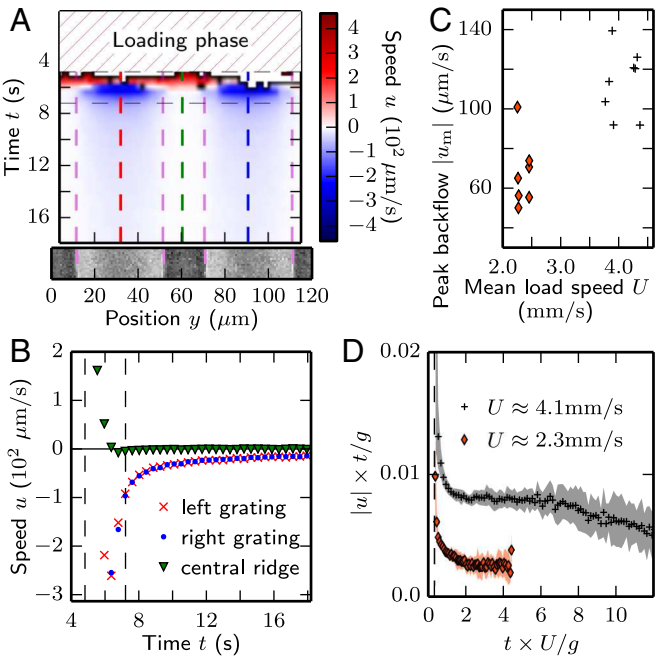

Fig. 4. Velocity measurements in pressure-relaxation experiments. (*A*) Kymograph showing the time evolution of the lateral profile of the midgap stream-wise velocity measured at ($x = g/2$, $z = -5\,\mu$m) after a constant loading speed $U \approx 4.1\,\text{mm}\cdot\text{s}^{-1}$. The two horizontal black dashed lines indicate the start and end of the pressure-head reduction to zero. *A*, *Bottom Inset* shows the position of the two gratings studied (appearing in light gray). The kymograph clearly shows a strong backflow over the lanes but not over the ridge (Movie S1). (*B*) Profiles from *A* taken along the red, blue, and green dashed vertical lines at the centerline of each grating and of the ridge, respectively. Red symbols are hidden by blue symbols as both gratings have the same profile. The SDs of all of the data are smaller than the symbol size. (*C*) Peak backflow velocity measured when the background pressure vanishes (corresponding to the second vertical dashed line in *B*), vs. the mean load speed for the two sets of experiments conducted for $U \approx 2.3\,\text{mm}\cdot\text{s}^{-1}$ and $U \approx 4.1\,\text{mm}\cdot\text{s}^{-1}$ (symbols as in D). (*D*) Ensemble average of the normalized backflow velocity multiplied by nondimensional time for the two sets of experiments, as a function of the nondimensional time. Standard deviations are shown in lighter shading.

We find that the maximum velocity of the backflow $|u_m|$, measured when the background pressure gradient vanishes ($t \approx 7$ s), increases with the magnitude of the mean load speed U, as shown in Fig. 4*C*. This is consistent with a sharpening of the concentration gradient near the downstream stagnation point at higher background pressure gradients during the loading phase, which then results in stronger Marangoni stresses driving the backflow. The observation that the plastron always displays a transient that reverses direction relating to the loading flow is a strong indication that Marangoni stresses are driven by surfactant accumulation, rather than by thermal gradients set up by laser or by other elements of the experimental apparatus (discussion in *SI Experimental Protocols*).

To provide additional support to the surfactant hypothesis, as well as to show that the occurrence of the backflow is largely independent of the type of surfactant (and therefore of the associated kinetics), we developed a model for the backflow and compare the resulting scaling for the plastron velocity to experimental results. As surfactant diffusion is initially negligible at the air–water interface compared with advection, we model the backflow using a one-dimensional time-dependent advection equation for the interfacial surfactant concentration (*SI Model for Pressure-Relaxation Experiments*). We assume adsorption/desorption fluxes are also negligible. These hypotheses

correspond to the stagnant cap regime (41). The surfactant transport equation is coupled with a viscous–Marangoni stress balance. Using a similarity solution, we find that the magnitude of the backflow decreases in time such that $|u| \propto 1/t$, which is in agreement with the experimental results plotted in Fig. 4*D* in nondimensional form. Fig. 4*D* shows the time evolution of the ensemble average (symbols) and SDs (light shadings) of the normalized backflow velocity $|u|/U$ multiplied by $t/(g/U)$. We show data for two sets of experiments conducted with $U \approx 2.3\,\mathrm{mm{\cdot}s^{-1}}$ and $U \approx 4.1\,\mathrm{mm{\cdot}s^{-1}}$ in the loading phase, plotted respectively in orange and black. The model is not valid at early time, $tU/g \leq 1$, due to the noninstantaneous decrease of the background pressure gradient occurring between the two vertical dashed lines, owing to the finite time required for the stage motion (≈3–4 s). At late times $tU/g \geq 6$, the plateau observed for the large forcing experiments seems to end, as the data decrease again. This is consistent with the fact that the model, which assumes a semi-infinite lane, is not valid at late times when the effect of the opposite stagnation point is felt. Moreover, we note in Fig. 4*D* that the value of the plateau region increases with U. This result contrasts with the model that predicts the backflow velocity depends only on the local concentration gradient. This indicates nonlinearities not taken into account by the model, such as strong variations in the initial surfactant distribution for different U or that the interface is not completely in the stagnant cap regime (discussion in *SI Model for Pressure-Relaxation Experiments*).

Outlook

An important conclusion is that quantitative models of superhydrophobic slip must also account for surfactant effects, or they can drastically overestimate drag reduction. This is consistent, for example, with established approaches for predicting the rise speed of small gas bubbles, which are known to be sensitive to surfactant-induced Marangoni stresses (41).

From a practical standpoint, our numerical and experimental findings point to the need to focus efforts on textures that have large distances between upstream and downstream stagnation points and that minimize locations where surfactant can accumulate. This explains why several experiments have reported that the greatest drag reduction was achieved with either long gratings (16, 42) or microposts or random textures having large gas fraction (up to 99%) (8, 12). Some of the largest slip lengths were achieved with annular gratings in a circular rheometer (12). Annular gratings are effectively infinitely long lanes, without stagnation points, thus preventing the formation of surfactant concentration gradient and adverse Marangoni stresses. However, applications of SHSs with annular geometries are limited. Textures with low gas fraction and small stream-wise interface length g (which can resist larger fluid pressure and can be easier to manufacture) have reported slip several times smaller than expected from surfactant-free theory (e.g., the meshes and posts in refs. 25 and 38 have gas fractions 26–55%; the gratings in ref. 24 have $g \simeq 1$ mm). In turbulent flows (such as in ref. 16) mixing is expected to enhance surfactant fluxes, potentially inducing a qualitative change in Marangoni stress. To enable general predictions, it would be important to extend existing effective slip models (27, 29, 34) to include surfactant.

From a methodological standpoint, our experimental tests involving pressure relaxation also provide a simple way of measuring the magnitude of surfactant-induced effects, for an SHS immersed in a given liquid. The presence of a backflow immediately reveals a plastron whose dynamics are strongly susceptible to surfactants. This can be a useful test to guide the design of SHSs that are unimpaired by surfactant Marangoni stresses. Overall, we believe this work constitutes a significant advance in our fundamental understanding of superhydrophobic drag reduction, moving the field closer to SHSs that perform reliably in realistic applications.

Materials and Methods

Numerical Simulations. The simulations solve six partial differential equations for the transport of mass, momentum, and surfactant in the fluid interior and along the air–water interface (41) (see *SI Model* for details). The ridges and bottom walls have a no-slip boundary condition. At the air–water interface we enforce continuity of the viscous stress with the Marangoni stress and continuity of the bulk velocity with the interfacial velocity. Air drag is negligible here and is not considered. Surfactants present in the interior layer near the plastron are adsorbed or desorbed following specific kinetics. We have chosen a well-characterized surfactant, namely SDS as our case study surfactant. The SDS properties are well described by Frumkin kinetics (39). These equations are solved using a finite-element method from COMSOL Multiphysics, with a Poiseuille profile as inlet condition and a weak constraint added to a free-slip boundary condition to capture the Marangoni effects at the air–water interface. A refined mesh at the interface and near the endpoints, together with higher-order elements, guarantees numerical accuracy (*SI Materials and Methods*).

Microchannel Preparation. Microchannels of PDMS (Sylgard 184) with a top surface consisting of long rectangular gratings were fabricated from a master mold obtained by photolithography (43) (*SI Experimental Protocols*). They were bonded to glass coverslips through untreated PDMS adhesion. All glass slides and tubing were washed thoroughly with purified water. The cleaning protocol is described in *SI Experimental Protocols*.

Laser Scanning Confocal Microscopy. To measure the fluid velocity, we washed and suspended microbeads (LifeTechnologies FluoSphere carboxylate 0.5-μm diameter yellow/green 505/515) in purified water (using the Milli Q water purification system; EMD Millipore) and injected the resulting solution at 0.08% solids in the chamber. Using a spinning-disk confocal microscope for green fluorescence (Yokogawa CSU-X1 mounted on a Zeiss Axio Observer Z1, with laser line 488 nm with power at the objective level less than 155 μW), we captured image sequences at distinct *z* planes of the chamber on a high-sensitivity EMCCD (Photometrics Evolve 512 Delta), at a rate of ≈10 frames per second. We used a water objective (Olympus LUMPLFLN 60XW) to guarantee a proper determination of the position of the imaging plane and allow deep imaging without loss of fluorescence brightness. A bright-field picture of the ridges and gratings allowed us to determine the position of the SHS with respect to the field of imaging. To prevent heating of the microchannel during imaging, it was placed in thermal contact with a heat-conducting plate, itself in contact with Peltier elements driven by a thermoelectric controller (Laird Technologies MTTC1410). To absorb the heat from the objective, we mounted a second Peltier element around it, coupled to a similar controller to maintain its temperature at 23± 0.1 °C. Fans were also used to cool the hot plates of the Peltier elements.

Flow Control. To ensure the driving pressure had no fluctuations, the flow of water with fluorescent particles was driven by gravity. The microchannel was connected with flexible tubing (Tygon ND-100-80) to two reservoirs (polypropylene tube; Eppendorf), whose absolute and relative heights could be varied independently. By varying the absolute position of the two reservoirs while keeping their relative position such that no flow was observable in the chamber, we minimized the curvature of the air–water interface in the chamber by adjusting the hydrostatic pressure. The maximum interface deflection over the width of the interface was less than 2 μm. By adjusting the relative position of the reservoirs, varying background pressure gradients could be imposed in the channel to generate flow. The variation of relative position was performed using a motorized stage (Thorlabs NRT150/M) driven by a precision controller (Thorlabs APT BSC201), guaranteeing a position precision of 2 μm and rapid changes in pressure gradients (maximum acceleration, 50 $\mathrm{mm{\cdot}s^{-2}}$; maximum speed, 50 $\mathrm{mm{\cdot}s^{-1}}$).

Image Analysis and μ-PIV. The images were analyzed with MATLAB, using a customized version of the PIV toolbox, mPIV (44). The correlation functions between adjacent frames were rescaled to correct for nonuniform time steps between frames, and the resulting correlation functions were added over a pack of 10–30 frames before searching for peak correlations. This allowed us to correct for Brownian motion uncertainties. For the time-relaxation experiments, the velocity profile in the chamber during the loading phase at high flow rate was obtained by measuring the mean length of the fluorescent particle streaks on the image and dividing by the exposure time.

ACKNOWLEDGMENTS. We thank D. Page-Croft and the engineers of the G. K. Batchelor Laboratory for their technical support. We gratefully acknowledge financial support from the Raymond and Beverly Sackler Foundation (R.E.G. and F.J.P.); the Engineering and Physical Sciences Research Council Grant 1196197 (to R.E.G. and F.J.P.); the European Research Council Grant 247333 (to R.E.G.); Mines ParisTech (F.J.P.); the Schlumberger Chair Fund (R.E.G.); and the University of California, Santa Barbara, Senate and California NanoSystems Institute Challenge Grant (to P.L.-F.); as well as from Churchill College (P.L.-F.) and Magdalene College (J.R.L.), Cambridge, United Kingdom.

1. Quéré D (2008) Wetting and roughness. *Ann Rev Mater Res* 38:71–99.
2. Rothstein JP (2010) Slip on superhydrophobic surfaces. *Ann Rev Fluid Mech* 42:89–109.
3. Samaha MA, Tafreshi HV, Gad-el Hak M (2012) Superhydrophobic surfaces: From the lotus leaf to the submarine. *C R Mécanique* 340:18–34.
4. Liu TL, Kim CJ (2014) Turning a surface superrepellent even to completely wetting liquids. *Science* 346:1096–1100.
5. Tian X, Verho T, Ras RHA (2016) Moving superhydrophobic surfaces toward real-world applications. *Science* 352:142–143.
6. Ou J, Perot B, Rothstein JP (2004) Laminar drag reduction in microchannels using ultrahydrophobic surfaces. *Phys Fluids* 16:4635–4643.
7. Ou J, Rothstein JP (2005) Direct velocity measurements of the flow past drag-reducing ultrahydrophobic surfaces. *Phys Fluids* 17:103606.
8. Choi CH, Kim CJ (2006) Large slip of aqueous liquid flow over a nanoengineered superhydrophobic surface. *Phys Rev Lett* 96:066001.
9. Joseph P, et al. (2006) Slippage of water past superhydrophobic carbon nanotube forests in microchannels. *Phys Rev Lett* 97:156104.
10. Tsai P, et al. (2009) Quantifying effective slip length over micropatterned hydrophobic surfaces. *Phys Fluids* 21:112002.
11. Karatay E, et al. (2013) Control of slippage with tunable bubble mattresses. *Proc Natl Acad Sci USA* 110:8422–8426.
12. Lee C, Choi CH, Kim CJ (2008) Structured surfaces for a giant liquid slip. *Phys Rev Lett* 101:064501.
13. Daniello RJ, Waterhouse NE, Rothstein JP (2009) Drag reduction in turbulent flows over superhydrophobic surfaces. *Phys Fluids* 21:085103.
14. Woolford B, Prince J, Maynes D, Webb BW (2009) Particle image velocimetry characterization of turbulent channel flow with rib patterned superhydrophobic walls. *Phys Fluids* 21:085106.
15. Jung YC, Bhushan B (2010) Biomimetic structures for fluid drag reduction in laminar and turbulent flows. *J Phys Condens Matter* 22:035104.
16. Park H, Sun G, Kim CJ (2014) Superhydrophobic turbulent drag reduction as a function of surface grating parameters. *J Fluid Mech* 747:722–734.
17. Lee C, Choi CH, Kim CJ (2016) Superhydrophobic drag reduction in laminar flows: A critical review. *Exp Fluids* 57:176.
18. Watanabe K, Udagawa Y, Udagawa H (1999) Drag reduction of Newtonian fluid in a circular pipe with a highly water-repellent wall. *J Fluid Mech* 381:225–238.
19. Gogte S, et al. (2005) Effective slip on textured superhydrophobic surfaces. *Phys Fluids* 17:051701.
20. Henoch C, et al. (2006) Turbulent drag reduction using superhydrophobic surfaces. *3rd AIAA Flow Control Conference* (American Institute of Aeronautics and Astronautics, Inc., Reston, VA).
21. Zhao J, Du X, Shi X (2007) Experimental research on friction-reduction with superhydrophobic surfaces. *J Mar Sci Appl* 6:58–61.
22. Peguero C, Breuer K (2009) On drag reduction in turbulent channel flow over superhydrophobic surfaces. *Advances in Turbulence XII*, ed Eckhardt B (Springer, Berlin), pp 233–236.
23. Kim TJ, Hidrovo C (2012) Pressure and partial wetting effects on superhydrophobic friction reduction in microchannel flow. *Phys Fluids* 24:112003.
24. Bolognesi G, Cottin-Bizonne C, Pirat C (2014) Evidence of slippage breakdown for a superhydrophobic microchannel. *Phys Fluids* 26:082004.
25. Gruncell B (2014) PhD thesis (University of Southampton, Southampton, UK).
26. Philip JR (1972) Flows satisfying mixed no-slip and no-shear conditions. *Z Angew Math Physik* 23:353–372.
27. Philip JR (1972) Integral properties of flows satisfying mixed no-slip and no-shear conditions. *Z Angew Math Physik* 23:960–968.
28. Cottin-Bizonne C, Barentin C, Charlaix É, Bocquet L, Barrat JL (2004) Dynamics of simple liquids at heterogeneous surfaces: Molecular-dynamics simulations and hydrodynamic description. *Eur Phys J E* 15:427–438.
29. Lauga E, Stone HA (2003) Effective slip in pressure-driven Stokes flow. *J Fluid Mech* 489:55–77.
30. Ybert C, Barentin C, Cottin-Bizonne C, Joseph P, Bocquet L (2007) Achieving large slip with superhydrophobic surfaces: Scaling laws for generic geometries. *Phys Fluids* 19:123601.
31. Sbragaglia M, Prosperetti A (2007) A note on the effective slip properties for microchannel flows with ultrahydrophobic surfaces. *Phys Fluids* 19:043603.
32. Teo CJ, Khoo BC (2010) Flow past superhydrophobic surfaces containing longitudinal grooves: Effects of interface curvature. *Microfluid Nanofluid* 9:499–511.
33. Davis AMJ, Lauga E (2009) Geometric transition in friction for flow over a bubble mattress. *Phys Fluids* 21:011701.
34. Crowdy DG (2016) Analytical formulae for longitudinal slip lengths over unidirectional superhydrophobic surfaces with curved menisci. *J Fluid Mech* 791:R7.
35. Kropfli RA, et al. (1999) Relationships between strong internal waves in the coastal zone and their radar and radiometric signatures. *J Geophys Res* 104: 3133–3148.
36. Lewis MA (1991) Chronic and sublethal toxicities of surfactants to aquatic animals: A review and risk assessment. *Water Res* 25:101–113.
37. Facchini MC, Decesari S, Mircea M, Fuzzi S, Loglio G (2000) Surface tension of atmospheric wet aerosol and cloud/fog droplets in relation to their organic carbon content and chemical composition. *Atmos Env* 34:4853–4857.
38. Schäffel D, Koynov K, Vollmer D, Butt HJ, Schönecker C (2016) Local flow field and slip length of superhydrophobic surfaces. *Phys Rev Lett* 116:134501.
39. Prosser AJ, Franses EI (2001) Adsorption and surface tension of ionic surfactants at the air–water interface: Review and evaluation of equilibrium models. *Colloids Surf A* 178:1–40.
40. Chang CH, Franses EI (1995) Adsorption dynamics of surfactants at the air/water interface: A critical review of mathematical models, data, and mechanisms. *Colloids Surf A* 100:1–45.
41. Palaparthi R, Papageorgiou DT, Maldarelli C (2006) Theory and experiments on the stagnant cap regime in the motion of spherical surfactant-laden bubbles. *J Fluid Mech* 559:1–44.
42. Truesdell R, Mammoli A, Vorobieff P, van Swol F, Brinker CJ (2006) Drag reduction on a patterned superhydrophobic surface. *Phys Rev Lett* 97:044504.
43. McDonald JC, Whitesides GM (2002) Poly(dimethylsiloxane) as a material for fabricating microfluidic devices. *Acc Chem Res* 35:491–499.
44. Mori N, Chang KA (2003) Introduction to mpiv. Available at www.oceanwave.jp/softwares/mpiv. Accessed May 15, 2015.
45. Rosen MJ, Kunjappu JT (2012) *Surfactants and Interfacial Phenomena* (Wiley, Hoboken, NJ).
46. Hourlier-Fargette A, Antkowiak A, Chateauminois A, Neukirch S (2017) Role of uncrosslinked chains in droplets dynamics on silicone elastomers. *Soft Matter* 13:3484–3491.

Supporting Information

Peaudecerf et al. 10.1073/pnas.1702469114

SI Model

Equations for Surfactant-Laden Flows. We consider a 2D microchannel flow over a finite-length SHS, with the geometry presented in Fig. 2*A*. Because we maintained a flat plastron in the experiments, and the present focus is on Marangoni stresses, here we assume that the air–water interface is flat.

The continuity and Navier–Stokes equations for the flow of mass and momentum are coupled with the transport equation for a surfactant. The 2D velocity field is $\boldsymbol{u} = (u, w)$ for the (x, z) directions, and the surfactant concentration field is c. The fluid has density ρ, as well as dynamic and kinematic viscosities μ and ν, respectively. The surfactant has bulk diffusivity D. The transport equations are, in dimensional form,

$$\nabla \cdot \boldsymbol{u} = 0, \qquad \textbf{[S1]}$$

$$\frac{\partial \boldsymbol{u}}{\partial t} + \nabla \cdot (\boldsymbol{u}\boldsymbol{u}) = -\frac{\nabla p}{\rho} + \nu \nabla^2 \boldsymbol{u}, \qquad \textbf{[S2]}$$

$$\frac{\partial c}{\partial t} + \nabla \cdot (\boldsymbol{u} c) = D \nabla^2 c. \qquad \textbf{[S3]}$$

The inlet and outlet conditions at $x = 0$ and $x = g + \ell$ respectively consist of a Poiseuille flow with mean velocity U and maximum velocity $u_{\max}$, such that

$$u(z) = 6U \, \frac{z}{H}\left(1 - \frac{z}{H}\right), \qquad \textbf{[S4]}$$

whereas the inlet has a specified bulk concentration $c = c_0$, and at the outlet we set

$$\frac{\partial c}{\partial x} = 0. \qquad \textbf{[S5]}$$

On the solid surfaces at $z = 0$ (top boundary or SHS side in Fig. 2*A*) and $z = -H$ (bottom boundary)

$$\boldsymbol{u} = \boldsymbol{0}, \qquad \textbf{[S6]}$$

$$\frac{\partial c}{\partial z} = 0. \qquad \textbf{[S7]}$$

At the plastron, an adsorption/desorption model is used to couple the surfactant transport between the bulk and the interface

$$D \left.\frac{\partial c}{\partial z}\right|_I = -S(c_I, \Gamma), \qquad \textbf{[S8]}$$

$$\frac{\partial \Gamma}{\partial t} + \frac{\partial (u_I \, \Gamma)}{\partial x} = D_{\mathrm{s}} \frac{\partial^2 \Gamma}{\partial x^2} + S(c_I, \Gamma), \qquad \textbf{[S9]}$$

where Γ is the interfacial concentration, D_{s} is the surface diffusivity, the subscript I denotes quantities at the interface, and $S(c_I, \Gamma)$ encapsulates the adsorption model. In practice, the choice of adsorption kinetics is of relatively weak importance, because surfactant effects are already very strong at extremely low surfactant concentrations (shown in Fig. 2 and Fig. S1). For such low values of concentration, different kinetics models are essentially equivalent (40). For definiteness, here we use Frumkin kinetics

$$S(c_I, \Gamma) = \kappa_{\mathrm{a}} c_I (\Gamma_{\mathrm{m}} - \Gamma) - \kappa_{\mathrm{d}} \, \Gamma \, \mathrm{e}^{A\Gamma/\Gamma_{\mathrm{m}}}, \qquad \textbf{[S10]}$$

where $\kappa_{\mathrm{a}}, \kappa_{\mathrm{d}}$ are the adsorption and desorption coefficients, Γ_{m} is the maximum packing interfacial concentration, and A is the interaction coefficient (39). On the air–water interface, the velocity field is coupled to the interfacial surfactant distribution through a balance between viscous and Marangoni stresses (45)

$$w = 0, \qquad \textbf{[S11]}$$

$$\mu \left.\frac{\partial u}{\partial z}\right|_I = -nRT \left(\frac{\Gamma_{\mathrm{m}}}{\Gamma_{\mathrm{m}} - \Gamma} + A \frac{\Gamma}{\Gamma_{\mathrm{m}}}\right) \frac{\partial \Gamma}{\partial x}, \qquad \textbf{[S12]}$$

where n is the surfactant style constant (40), R is the universal gas constant, and T is the absolute temperature. The boundary condition for Γ, where the interface meets each solid boundary at a stagnation point on the top boundary $z = 0$ (i.e., upstream stagnation point, $x = \ell/2$, and downstream stagnation point, $x = g + \ell/2$; Fig. 2*A*), is given by

$$\frac{\partial \Gamma}{\partial x} = 0. \qquad \textbf{[S13]}$$

We can nondimensionalize Eqs. **S1**–**S3**, **S9**, and **S10** and the boundary conditions **S4**–**S8** and **S11**–**S13** to reveal nine characteristic nondimensional numbers for this problem. Using g as a characteristic length scale, U as a characteristic velocity scale, g/U as a characteristic time scale, ρU^2 as a characteristic pressure scale, c_0 as a characteristic bulk concentration scale, and Γ_{m} as a characteristic interfacial concentration scale, we obtain the nondimensional conservation equations for mass, momentum, bulk surfactant, and interfacial surfactant (where hats denote nondimensional quantities),

$$\nabla \cdot \hat{u} = 0, \qquad \textbf{[S14]}$$

$$\frac{\partial \hat{u}}{\partial \hat{t}} + \nabla \cdot (\hat{u}\hat{u}) = -\nabla \hat{p} + \frac{\hat{H}}{Re} \nabla^2 \hat{u}, \qquad \textbf{[S15]}$$

$$\frac{\partial \hat{c}}{\partial \hat{t}} + \nabla \cdot (\hat{u}\hat{c}) = \frac{1}{Pe} \nabla^2 \hat{c}, \qquad \textbf{[S16]}$$

$$\frac{\partial \hat{\Gamma}}{\partial \hat{t}} + \frac{\partial (\hat{u}_I \hat{\Gamma})}{\partial \hat{x}} = \frac{1}{Pe_{\mathrm{s}}} \frac{\partial^2 \hat{\Gamma}}{\partial \hat{x}^2} + \hat{S}(\hat{c}_I, \hat{\Gamma}), \qquad \textbf{[S17]}$$

where the source–sink concentration flux at the interface is

$$\hat{S}(\hat{c}_I, \hat{\Gamma}) = Bi \left[k \hat{c}_I (1 - \hat{\Gamma}) - \mathrm{e}^{A\hat{\Gamma}} \hat{\Gamma}\right]. \qquad \textbf{[S18]}$$

At the inlet $\hat{x} = 0$, the boundary conditions are, in nondimensional form,

$$\hat{u} = \frac{6\hat{z}}{\hat{H}}\left(1 - \frac{\hat{z}}{\hat{H}}\right), \qquad \textbf{[S19]}$$

$$\hat{w} = 0, \qquad \textbf{[S20]}$$

$$\hat{c} = 1. \qquad \textbf{[S21]}$$

At the outlet $\hat{x} = 1 + \hat{\ell}$,

$$\hat{u} = \frac{6\hat{z}}{\hat{H}}\left(1 - \frac{\hat{z}}{\hat{H}}\right), \qquad \textbf{[S22]}$$

$$\hat{w} = 0, \qquad \textbf{[S23]}$$

$$\frac{\partial \hat{c}}{\partial \hat{x}} = 0. \qquad \textbf{[S24]}$$

On the solid surfaces at $\hat{z} = 0$ and $\hat{z} = -\hat{H}$,

$$\hat{u} = \boldsymbol{0}, \qquad \textbf{[S25]}$$

$$\frac{\partial \hat{c}}{\partial \hat{z}} = 0. \qquad \textbf{[S26]}$$

On the air–water interface at $\hat{z} = 0$, $\hat{\ell}/2 \le \hat{x} \le \hat{\ell}/2 + 1$,

$$\hat{w} = 0, \qquad \textbf{[S27]}$$

$$\left.\frac{\chi k}{Pe}\frac{\partial \hat{c}}{\partial \hat{z}}\right|_I = -\hat{S}(\hat{c}_I, \hat{\Gamma}), \quad \textbf{[S28]}$$

$$\left.\frac{\partial \hat{u}}{\partial \hat{z}}\right|_I = -Ma\left(\frac{1}{1-\hat{\Gamma}} + A\hat{\Gamma}\right)\frac{\partial \hat{\Gamma}}{\partial \hat{x}}, \quad \textbf{[S29]}$$

$$\frac{\partial \hat{\Gamma}}{\partial \hat{x}} = 0 \quad \text{at } \hat{x} = \hat{\ell}/2,\ 1+\hat{\ell}/2. \quad \textbf{[S30]}$$

The Reynolds number is $Re = HU/\nu$, based on the transverse length scale H instead of the longitudinal length scale g. For the internal channel flow considered in this study, H is the appropriate length scale to determine the flow regime, which is Stokes flow ($Re \lesssim 1$) for all our experiments and numerical simulations. The bulk and surface Péclet numbers are $Pe = gU/D$ and $Pe_s = gU/D_s$. The nondimensional bulk concentration is $k = \kappa_a c_0/\kappa_d$. The Biot number is $Bi = \kappa_d g/U$. The kinetics are parameterized by $\chi = \kappa_d g/(\kappa_a \Gamma_\infty)$. The Marangoni number is $Ma = nRT\Gamma_\infty/(\mu U)$. We note that there are also two geometrical nondimensional numbers: the aspect ratio of the channel $\hat{H} = H/g$ and the proportion of solid surface to free surface on the SHS side $\hat{\ell} = \ell/g$. With nine nondimensional parameters, of which six depend on the physical and kinetic properties of the surfactant, the full transport problem related to surfactant-contaminated SHSs is effectively very complex.

The nondimensional numbers of all our experiments and simulations are presented in Tables S2, S4, and S7. We have also computed two other useful nondimensional ratios (41): $\mathcal{D} = \chi(1+k)/Pe^{1/2}$, the ratio of the diffusive flux of surfactants across the diffusive boundary layer to the convective flux along the air–water interface (which is based on [**S16**] at steady state), and $\mathcal{K} = Bi(1+k)$, the ratio of the adsorption/desorption kinetics flux to the convective flux along the interface (which is based on [**S18**]). A discussion of the scaling analysis of the equations above and their characteristic nondimensional numbers is provided in *SI Analysis and Discussion of Characteristic Nondimensional Numbers*.

SI Materials and Methods

Two-Dimensional Surfactant-Laden Simulations. The model presented above was implemented in COMSOL Multiphysics in a 2D finite-element numerical simulation. The geometry corresponding to Fig. 2*A* was created using the values for the gap length g, the ridge length ℓ, the chamber height H, and the maximum forcing speed of the Poiseuille flow u_{max} presented in Table S1. All other relevant physical and kinetic parameters of the simulations are presented in Table S1 and correspond to the well-characterized surfactant SDS. Note that in *Supporting Information*, we use interchangeably mol·m^{-3} and mM as equal units for surfactant bulk concentrations. The SDS properties are well described by Frumkin kinetics (39). Nondimensional numbers associated with these 2D simulations are listed in Table S2.

When designing the mesh of the domain, we were particularly careful about strong possible variations of some variables near the stagnation points at the beginning and end of the gap. The maximum size of elements near these points is equal to 0.01 μm. For all simulations with $g < 1$ mm, the maximum element size on the interface is 0.05 μm. For simulations with $g = 1$ mm and 2 mm, the maximum element size on the interface is 0.2 μm. Finally, for $g = 5$ mm and 10 mm, a coarser mesh is used in the central part of the interface, 1 mm away from the endpoints, with a maximum element size of 2 μm. In the bulk, the maximum element size is 10 μm for all simulations.

To implement the model, we combine the laminar flow module with a dilute species transport module of COMSOL for the transport equations in the bulk (Eqs. **S1**–**S3**). The equation for the transport of surfactant on the interface (Eq. **S9**) is implemented through a general form boundary partial differential equation, with a source term corresponding to the kinetics flux S. This flux also serves to implement the boundary condition **S8** at the interface for the dilute species transport module. The Marangoni forces resulting from the nonuniform distribution of surfactants at the interface modify the laminar flow, as stated in [**S12**], through a weak contribution at the interface coupled to a free-slip boundary condition.

The flow in the simulated chamber is forced by an inlet velocity boundary condition corresponding to a Poiseuille velocity profile $u(z) = 4u_{max}z(H-z)/H^2$ (with $u_{max} = 3U/2$). The initial guess velocity profile for the stationary solver is set to this reference Poiseuille profile in the entire chamber.

To increase the accuracy of the computation, we discretize the fluid flow with quadratic elements for the velocity field and linear elements for the pressure field and quadratic elements for the concentration field in the bulk and the concentration field on the interface.

We use the MUMPS solver of COMSOL to solve for the steady state of the system, with a relative tolerance of 10^{-5}.

To check how the results obtained would change for surfactants of different strengths, we also ran simulations for two extreme sets of parameters values for the surfactant choice, using the Frumkin kinetics framework (Fig. S1). The first set corresponds to a model of strong surfactant with high affinity to the interface and low diffusivity ($\kappa_d = 1\,s^{-1}$, $\kappa_a = 10^6\,m^3{\cdot}mol^{-1}{\cdot}s^{-1}$, $\Gamma_\infty = 10^{-5}$ mol·m^{-2}, $A = -3$, $D = D_s = 10^{-11}\,m^2{\cdot}s^{-1}$), the second set corresponds to a model of weak surfactant with weak affinity to the interface and high diffusivity that promotes the smoothing of any interfacial gradients ($\kappa_d = 100\,s^{-1}$, $\kappa_a = 10^{-1}\,m^3{\cdot}mol^{-1}{\cdot}s^{-1}$, $\Gamma_\infty = 10^{-6}$ mol·m^{-2}, $A = 3$, $D = D_s = 10^{-9}\,m^2{\cdot}s^{-1}$). These parameters were typically selected from the extreme values of the data reported in tables 1 and 3 in ref. 40. We performed simulations with the rest of the parameters as in the simulation for Fig. 2*D*, except for the bulk concentration c_0 whose range was extended to cover the transitions for the strong and weak surfactants, respectively (see Tables S1 and S2 for all of the parameter values and associated nondimensional numbers, respectively). For both cases, we observe progressive immobilization of the interface and increase of viscous stress with increasing bulk concentration of surfactant (Fig. S1). For the strong surfactant (plotted with blue symbols), the transition toward a no-slip boundary condition occurs at minute concentrations, below $c_0 \approx 10^{-12}$ mM and well below the transition value for SDS ($c_0 \approx 10^{-4}$ mM). For the weak surfactant (plotted with green symbols), the transition occurs at $c_0 \approx 1$ mM, which is much higher than for SDS. In general, one cannot of course guarantee that no traces of strong surfactants are present in a given flow.

Three-Dimensional Surfactant-Free Simulations. To obtain a reference flow profile for long rectangular gratings located on one side of a 3D microchannel, in the idealized case of pure water ($c_0 = 0$), we solved the Navier–Stokes equations using COMSOL Multiphysics. The aim is to compare these clean-case or surfactant-free simulations with the two steady-state forcing experiments shown in Fig. 3 *D* and *E* with symbols (numerical results are shown with solid lines). Our 3D numerical domain corresponds to the portion of a microchannel below half of a grating element, with plane of symmetry $(x, y = w/2, z)$ (Fig. 2 *B* and *C*). We use symmetry boundary conditions on each side of the domain to solve for the flow on a large number of parallel gratings as in the experiment. All of the parameters for these two simulations, with $g = 2$ mm and 30 mm in Fig. 3 *D* and *E*, respectively, are detailed in Table S5. The numerical parameters are chosen to match the experimental conditions, assuming a surfactant-free flow. No-slip boundary conditions are imposed on the ridges, whereas free slip is imposed on the plastron. The flow

was forced by a 2D Poiseuille profile $u(z) = 4u_{\max} z(H - z)/H^2$ with $u_{\max} = 120\ \mu m \cdot s^{-1}$. All of the experiments being conducted at low Reynolds number in the Stokes regime, we note that the normalized velocity profiles presented in Fig. 3 *D* and *E* do not depend on $u_{\max}$ or U. This same velocity profile was also chosen as an initial guess for the steady-state solution. Water viscosity was $\mu = 9.3 \times 10^{-4}\ N \cdot s \cdot m^{-2}$, corresponding to the water temperature of 23 °C measured in the laboratory during the steady-state forcing experiments. We use a Physics-controlled mesh with finer to extrafine element size, with a linear discretization of elements and further local refinement of meshing around the areas of interest if required.

SI Experimental Protocols

Cleaning Protocols. Two different cleaning protocols were followed in the preparation of the experiments. For both cleaning protocols, as well as all of the experiments conducted, only purified water (using the Milli Q water purification system; EMD Millipore) at 23 °C with resistivity 18.2 MΩ·cm and less than 5 parts per billion of total organic content was used.

A strict 10-d cleaning protocol was designed in an attempt to avoid any contamination of the microchannel, which could induce surfactant Marangoni stresses. The cleaning and experimental preparation were performed using laboratory coats and thoroughly washed nitrile gloves (Fisherbrand) (we note that standard laboratory gloves have traces of chemicals on their surface, which induce surfactant Marangoni stresses). The preparation of the PDMS (Sylgard 184) microchannels was done in a clean room. In this protocol, apart from the PDMS, only materials that could be cleaned thoroughly were used for the surfaces that were in contact with water during the experiments. In particular, all common plastic materials were avoided as they tend to release chemical traces with a surfactant effect when in contact with water. All tubings were made of fluorinated ethylene propylene (FEP) (0.5 mm internal diameter; The Dolomite Center Ltd.), connectors were made of stainless steel, the syringes (Gastight Hamilton) used to handle water and the microbead suspension were made of glass and polytetrafluoroethylene and fitted with stainless steel needles (24-gauge injection needles; Carl Roth GmbH), and the inlet and outlet reservoirs were made of glass. All of the tubings, connectors, needles, and reservoirs underwent five washing, rinsing, and curing cycles over a 10-d period before the experiments. The curing containers were large glass beakers that had been cleaned in an acid rinse dishwasher and further rinsed for 5 min with purified water. During the curing process, all of the beakers were covered to reduce contamination from the air. On the day of the experiments, all of the tubings and reservoirs were washed again with purified water. Washed metal tweezers were used to handle tubings and connectors to avoid touching surfaces that could be in contact with the water flowing through the microchannel. The fluorescent microbeads (LifeTechnologies FluoSphere carboxylate 0.5-μm diameter yellow/green 505/515) used to perform μ-PIV were washed and rinsed 10 times with purified water to dilute significantly any potential surfactant contamination traces. The coverslip forming the base of the microchannel was washed with abundant purified water and then air dried.

This strict cleaning protocol was followed only when conducting some steady-forcing experiments. The results, similar to those presented in Fig. 3*D* (conducted following the normal cleaning protocol described below), showed no or little slip in comparison with theoretical and numerical predictions with surfactant-free flows. As we show in Fig. 2*D*, the level of contamination necessary to induce surfactant Marangoni stresses is extremely small, of the order of 10^{-4} mM for the SDS surfactant. Moreover, as we show in Fig. S1, SDS is not the strongest surfactant and can be considered as inducing mild Marangoni stresses (see tables 1 and 3 in ref. 40, for a comparison of a broad range of surfactants). Therefore, it is very likely that, even following this strict cleaning protocol, sufficient traces of chemicals with a surfactant effect contaminated our experiments. We believe that the most likely source of contamination in our experiments is the PDMS and its associated impurities. Un–cross-linked PDMS chains or impurities trapped in the PDMS could have a surfactant effect as has been observed in ref. 46. Contamination could also come from other sources, which might simply be unavoidable in normal laboratory conditions.

As surfactant contaminations were simply unavoidable in our experiments, a less time-consuming cleaning protocol was used for all of the experimental results presented in this study. We used flexible tubing (Tygon ND-100-80) instead of the FEP tubing, which was more difficult to handle due to its rigidity. The outlet and inlet reservoirs were replaced by polypropylene tubes (Eppendorf) or plastic syringes (BD Plastipack). All of the other elements of the apparatus, preparation tools, and materials were the same. Furthermore, cleaning of the tools, materials, tubings, connectors, and reservoirs was performed on the day of the experiment. They were all washed with plenty of purified water: typically with at least 10 times the volume they can contain. The fluorescent microbeads were washed at least 3 times.

Steady-Forcing Experiments. For steady-forcing experiments, the chamber was first filled with the suspension of microbeads, taking great care to avoid trapping any air bubble in the tubing or in the chamber. To obtain a low level of flow rate in the chamber while allowing accurate positioning of the inlet reservoir with respect to the outlet reservoir, a constriction was introduced on the hydraulic line by mounting a 30-gauge polypropylene syringe tip (Adhesive Dispensing Ltd.) on the inlet reservoir (syringe from BD Plastipack). Using a manual linear stage, the inlet reservoir was moved vertically after initial filling of the chamber until no flow could be observed in the middle of the chamber. This corresponded to the level of zero pressure gradient along the microfluidic line. The inlet position was then shifted by 5 mm ± 10 μm, using the linear manual stage. Imaging was then performed in the central longitudinal portion of the gratings. Stacks of 30 successive images were taken at ≈10 fps at different z positions in the chamber and at different time points for each experiment. Once a microchannel was successfully prepared to conduct a series of experiments, most of the plastrons of the SHS gratings remained stable for ≈2 h.

The details of the parameters for the experiments presented in Fig. 3 *D* and *E* are described in Table S3. All of the nondimensional numbers associated with these experiments are presented in Table S4. As the type of surfactant that contaminated these experiments is unknown, we have assumed the same properties as the weak and strong surfactants whose physical and kinetics properties are described in Table S1. We have also assumed a broad concentration range for both surfactants, from $10^{-12}\ mol \cdot m^{-3}$ to $1\ mol \cdot m^{-3}$. This gives us a broad range of values for the different nondimensional numbers. The mean forcing speed U was calculated from the experimental velocity profile by fitting a parabolic profile $u(z) = 6Uz(H - z)/H^2$ to the data.

Pressure-Relaxation Experiments. The protocol for each experiment had two phases: an initial loading phase with strong background flow and then a second phase without background flow to measure the surfactant Marangoni-driven backflow. During the initial loading phase the flow was driven at a very high background pressure gradient, to transport any surfactant along the air–water interface to the downstream stagnation end of a grating. This phase lasts for 4 min, during which images of the flow field were taken at different heights in the channel to obtain the vertical distribution of the stream-wise velocity profile. A typical velocity profile measured during the loading phase of the experiment shown in Fig. 4*A* is presented in Fig. S2. As the exposure

time on the camera was smaller but of the same order of magnitude as the typical time for the fluorescent particles to cross the field of view, particles were seen as streaks of dots on each image. The dots forming the streaks originate from the imaging by the spinning disk used with the microscope. The velocity profile was obtained by measuring the mean length of the fluorescent particle streaks on the image and dividing by the exposure time. As we can see in Fig. S2, the velocity profile measured in a vertical plane centered in the middle of a grating does not show any significant slip velocity at the air–water interface. We note that the spatial resolution and the technique to measure the velocity were not designed to measure accurately the velocity close to the plastron, as was done in the steady-forcing experiments (previous section and Fig. 3). The aim here was to obtain an estimate of the mean flow field in the microchannel. The profile follows a classical 2D Poiseuille profile, from which we computed the mean load speed U plotted in Fig. 4*C*.

In the second phase, the background pressure gradient was suppressed to stop the flow. Images of the flow field were recorded at a distance of $z = -4\,\mu\text{m} \pm 1\,\mu\text{m}$ from the air–water interface. Images were recorded for 1 min or 2 min starting ≈5 s before the background pressure gradient was suppressed (this corresponds to $t = 0$ in Fig. 4 *A*, *B*, and *D*), at a frame rate of around 24 frames per second. See the snapshot corresponding to Movie S1 as an example. These images were then analyzed with μ-PIV, as explained in *Materials and Methods*, to produce the velocity fields, such as the one displayed in Fig. 4*A*. Then, the experiment was repeated but with imposing a negative background pressure gradient in the microchannel to produce an opposite flow. We could thus verify that the effect observed was independent of the flow direction in the initial loading phase.

The apparatus and the microchannels were prepared following the initial steps of the protocol described in the previous section. Then, to control the background pressure gradient imposed in the microchannel during the loading phase and ensure a rapid and smooth transition between the two phases, the inlet reservoir was attached at midheight onto a 150-mm motorized stage (Thorlabs NRT150/M) driven by a precision controller (Thorlabs APT BSC201, with 2 μm precision; maximum acceleration, 50 $\text{mm}\cdot\text{s}^{-2}$; maximum speed, 50 $\text{mm}\cdot\text{s}^{-1}$). This midheight constituted our zero elevation reference. The outlet reservoir was attached onto the fixed part of the motorized stage, which was itself attached onto a millimetric precision vertical ramp. Adjusting the height of the motorized stage effectively controlled the hydrostatic pressure in the microchannel and thus the interfacial deflection of the plastron. An initial upward loading phase was conducted, without recording any images, to determine accurately the level of zero background pressure gradient required for the second phase. Indeed, during this first loading phase where the inlet reservoir was raised to a given height ($\Delta H_r > 0$) compared with the outlet reservoir, water transferred from the inlet reservoir to the outlet reservoir. This led to a slight increase in the neutral elevation of the inlet reservoir corresponding to a zero background pressure required for the second phase. Then, to avoid complete depletion of the inlet reservoir by having flow in one direction only for all of the experiments, the next loading phase was conducted with a flow in the opposite direction, by lowering the inlet reservoir to a negative or opposite elevation ($\Delta H_r < 0$) of the exact same distance as in the upward loading phase. At the end of this first downward loading phase, which also lasts exactly 4 min, the inlet reservoir could simply be returned to the original zero reference elevation, having transferred back to the inlet reservoir the same amount of water that was depleted during the upward loading phase. The neutral elevations at the end of the upward and downward loading phases were found with an accuracy of 2–3 μm, which produced a very small flow below the level of detection of the μ-PIV system. This cycle was then repeated four times, with images recorded during the loading phase to measure the velocity of the backflow.

The experimental parameters of all of the pressure-relaxation experiments are presented in Table S6. All of the nondimensional numbers associated with these experiments are presented in Table S7. Similar to the steady experiments, as the type of surfactant that contaminated these experiments is unknown, we have assumed the same properties as the weak and strong surfactants whose kinetics properties are described in Table S1. We have also assumed a broad concentration range for both surfactants, from $10^{-12}\,\text{mol}\cdot\text{m}^{-3}$ to $1\,\text{mol}\cdot\text{m}^{-3}$. This gives us a broad range of values for the different nondimensional numbers. Note that by convention the background flow mean speed U is always considered positive, independently of the flow direction in the microchannel, so that the backflow is always negative, as shown in Fig. 4 *A* and *B*. To indicate whether the loading phase was conducted upward or downward, ΔH_r is shown as positive or negative, respectively. As can be noted, there is a small asymmetry of $\sim\pm 5\%$ between the mean flow speeds of an upward loading phase and a downward loading phase. This is due to a different spatial arrangement of the tubings between the two loading phases. We also note that not all experiments could be exploited quantitatively. Due to the strong pressure change at the end of the loading phase, the plastron of some gratings failed and led to their wetting. Wetting could affect either the grating under study or an adjacent grating (notes in Table S6). With adjacent grating failure, the backflow was still observed on the remaining plastron, with qualitatively similar magnitude and time scale, but the backflow velocity was affected through viscous stresses in the water. These data were therefore not quantitatively accurate and have not been included in the graphs presented in Fig. 4 *C* and *D*. The contrast between the flow field of a nonwetted grating and that of a wetted grating is also very clear when stopping the background pressure gradient. Similar to the flow above a ridge, the flow in the wetted grating stops immediately at the end of the loading phase, showing no backflow (Movie S2, which corresponds to Experiments 2-4 in Table S6).

Impact of Thermal Marangoni Effects in Experiments. We assess the potential impact of thermal Marangoni effects in our experiments to examine whether the backflow observed in the pressure-relaxation experiments could be due to thermal Marangoni effects. We distinguish steady temperature gradients from flow-dependent gradients.

Steady temperature gradients can arise due to spatial temperature variations in the setup close to the microchannel. As the backflow was observed in both flow directions through the microchannel, within a few minutes' interval, this implies that a steady spatial temperature gradient did not affect the experiments.

Temperature gradients could also arise due to heat being advected by the flow during the loading phase. This heat could come from the laser, although we note that its power was already very small, less than 155 μW, and only a small fraction would have been absorbed as heat by water. As the microchannel height is only $H \approx 0.1\,\text{mm}$, the time scale for thermal diffusion across H is of the order of $H^2/D_T \approx 0.1\,\text{s}$, where $D_T \approx 1.4 \times 10^{-7}\,\text{m}^2\cdot\text{s}^{-1}$ is the thermal diffusivity of water. Because the bottom of the microchannel is maintained at a fixed temperature by a Peltier element, as soon as the loading phase ends the temperature variations in the microchannel should vanish within ∼0.1 s. However, the time scales for the backflow are typically of the order of 1 min. Therefore, thermal Marangoni effects had negligible impact in our experiments.

SI Analysis and Discussion of Characteristic Nondimensional Numbers

The problem of surfactant-contaminated SHSs is a complex transport problem involving several coupled nonlinear partial

differential equations (Eqs. **S14–S17**). In addition, at the air–water interface a flux continuity condition **S28** couples the bulk concentration and the interfacial concentration, and a stress continuity condition **S29** couples the viscous force and the interfacial concentration gradient (i.e., Marangoni effect). To understand the effects of geometry, surfactant concentration or changes in surfactant properties on the drag reduction performance of the SHS through the scaling analysis of these equations is therefore a nontrivial exercise. Nevertheless, a few remarks can be made to explain, at least qualitatively, the main results of our study. The key results are that (*i*) only very small amounts of surfactants are needed to drastically reduce the drag reduction performance of SHSs (shown numerically and suggested by our careful experimental trial) and (*ii*) free slip at the air–water interface can be recovered when increasing the length of the gap g (shown numerically and experimentally).

From [**S29**], the air–water interface becomes a no-slip boundary if the velocity gradient at the interface scales as $\partial\hat{u}/\partial\hat{z} \sim 1/\hat{H}$ (with $\hat{H} = H/g$). Assuming that the interfacial concentration gradient scales as $\partial\hat{\Gamma}/\partial\hat{x} \sim \langle\hat{\Gamma}\rangle$ (with $\langle\hat{\Gamma}\rangle$ the average concentration over the gap), we find that

$$\langle\hat{\Gamma}\rangle \sim \frac{g}{HMa}. \qquad \textbf{[S31]}$$

Even when assuming extremely weak surfactant properties, the Marangoni number is very large in all our experiments and numerical simulations, $Ma \sim 10^3$–10^6. We note that Ma is based on the maximum packing concentration Γ_m instead of a measure of the actual interfacial concentration, which is unknown. Hence, Ma represents the maximum possible value in the limit $\hat{\Gamma} \to 1$. Large Ma values imply that no slip at the interface can be achieved for $\langle\hat{\Gamma}\rangle \ll 1$. Although the relationship between the c_0 and Γ is rather complex through the diffusive boundary layer, the kinetics flux, and various couplings, this suggests that the threshold for the bulk surfactant contaminant c_0 is also very small. This is in agreement with our key finding *i*. Also, [**S29**] and [**S31**] show that increasing the gap length g, while maintaining all other parameters constant, will eventually lead to an increase in slip at the SHS. This is in agreement with our key finding *ii*.

Eqs. **S29** and **S31** suggest a linear relationship between the slip velocity at the interface and the interfacial concentration, at least for low $\langle\hat{\Gamma}\rangle$. However, we have found in Fig. 2*D* and [**S1**] that the transition from no slip to free slip at the SHS is strongly nonlinear, regardless of the type of surfactant. Similarly, the transition due to changes in gap length shown in Fig. 2*E* is also nonlinear. This is characteristic of the strong nonlinear couplings between the velocity field, the bulk concentration, and the interfacial concentration in this problem. It also shows the limits of our scaling analysis, where we assumed a simple linear profile for Γ. The authors of ref. 41 describe the different regimes for the surfactant concentration distribution at the interface of air bubbles rising in surfactant-contaminated water. Their axisymmetric problem is similar to our 2D problem, considering the top and bottom of the bubble as the upstream and downstream stagnation points of our SHS. The regimes they describe, based on the surfactant-related nondimensional parameters, relate the interfacial surfactant distribution with the flow at the macroscopic scale. If $\mathcal{D} \sim 1$ and $\mathcal{K} \sim 1$ [where $\mathcal{D} = \chi(1+k)/Pe^{1/2}$ is the ratio of the diffusive flux of surfactants across the diffusive boundary layer to the convective flux along the interface, and $\mathcal{K} = Bi(1+k)$is the ratio of the adsorption/desorption kinetics flux to the convective flux along the interface], then the interfacial concentration gradient is approximately uniform (i.e., the concentration profile is linear) along most of the interface. This is known as the "uniformly retarded regime." If $\mathcal{D} \ll 1$ or $\mathcal{K} \ll 1$ and $Pe_s \gg 1$, the interface is in the stagnant cap regime, characterized by a depletion of surfactant in the upstream part of the interface, a sharp nonlinear increase of the interfacial concentration, and an accumulation of surfactant near the downstream stagnation point.

According to the results displayed in Table S2, all our numerical simulations (Fig. 2 and Fig. S1) are in a transition regime between the uniformly retarded regime and the stagnant cap regime, except for the strong model surfactant (Fig. S1) that is in the stagnant cap regime. This means that the surfactant distribution is neither constant nor linear along the interface. Marangoni stresses can therefore develop due to concentration gradients along the interface in all our experiments.

Although the type of surfactants and their concentration are unknown in all our experiments (Figs. 3 and 4), we have estimated ranges for all of the nondimensional numbers in Tables S4 and S7, using the physical and kinetics properties of the weak and strong model surfactants described in Table S1 and assuming a broad range of concentration from $c_0 = 10^{-12}$ to $1\,\mathrm{mol{\cdot}m^{-3}}$. The dimensional numbers show that all our experiments are most likely in a transition regime, similar to the results found for our numerical simulations. Only if the contaminant present in our experiments had the same properties as the strong model surfactant and its concentration was less than $\approx 0.1\,\mathrm{mol{\cdot}m^{-3}}$ would the experiments be in the stagnant cap regime. Thus, the numerical simulations with SDS as contaminant appear to be an appropriate model for this problem.

Therefore, the analysis of the nondimensional characteristic numbers confirms the main conclusions of our study. Surfactant contaminants at very small concentrations can induce Marangoni stresses at the air–water interface of the SHS through a nonuniform concentration distribution established by the flow. The surfactant distribution is most likely in a nonlinear transition regime between the uniformly retarded regime and the stagnant cap regime. Marangoni stresses at the SHS can be reduced if the distance between the two stagnation points is larger than a critical value, which appears to be a nonlinear function of the interfacial concentration distribution, the Marangoni number, and the channel height.

SI Model for Pressure-Relaxation Experiments

We develop a model that predicts the temporal scale for the rapid backflow that we observed in the pressure-relaxation experiments (Fig. 4). We consider the geometry described in Fig. 2*A*, with the flow in the loading phase in the positive direction. We assume that the backflow observed at the end of the loading phase and developing in the negative direction is dominated by advection and thus neglect diffusion along the interface and the adsorption–diffusion flux between the interface and the bulk. These assumptions correspond to the stagnant cap regime where $Pe_s \gg 1$ and $\mathcal{D} \ll 1$ or $\mathcal{K} \ll 1$, which is possible in our experiments if the surfactant contaminants are strong and in relatively low concentrations. This is possible if contaminants are only hydrophobic PDMS chains. We solve the one-dimensional time-dependent advection equation for the transport of surfactants at the interface. Eq. **S17** simplifies to, in nondimensional form,

$$\frac{\partial\hat{\Gamma}}{\partial\hat{t}} + \frac{\partial(\hat{u}_I\hat{\Gamma})}{\partial\hat{x}} = 0. \qquad \textbf{[S32]}$$

In addition, because $Re = UH/\nu \ll 1$, viscous spreading across the channel height occurs very quickly compared with surfactant advection, and we approximate $(\partial\hat{u}/\partial\hat{z})_I$ as $\hat{u}_I/\hat{H}$ in the left-hand side of [**S29**]. Given that the surfactant concentration is very small, $\hat{\Gamma} \ll 1$, the right-hand side of [**S29**] can be linearized to give

$$\frac{\hat{u}_I}{\hat{H}} = -Ma\frac{\partial\hat{\Gamma}}{\partial\hat{x}}. \qquad \textbf{[S33]}$$

Substituting $\hat{u}_I$ from [**S33**] into [**S32**], we find the conservation equation for $\hat{\Gamma}$:

$$\frac{\partial \hat{\Gamma}}{\partial \hat{t}} - Ma\hat{H}\frac{\partial}{\partial \hat{x}}\left(\hat{\Gamma}\frac{\partial \hat{\Gamma}}{\partial \hat{x}}\right) = 0. \qquad \textbf{[S34]}$$

We introduce the similarity variables

$$\eta = \frac{1+\hat{\ell}/2-\hat{x}}{\left(\hat{t}Ma\hat{H}\right)^{1/3}}, \qquad \textbf{[S35]}$$

$$\hat{\Gamma}(x,t) = \left(\hat{t}Ma\hat{H}\right)^{-1/3} f(\eta). \qquad \textbf{[S36]}$$

Substituting into [**S34**], integrating twice, and using the boundary condition **S30**, the solution is

$$\hat{\Gamma}(x,t) = \frac{C}{\left(\hat{t}Ma\hat{H}\right)^{1/3}} - \frac{\left(1+\hat{\ell}/2-\hat{x}\right)^2}{6\hat{t}Ma\hat{H}}, \qquad \textbf{[S37]}$$

which is valid for $\hat{t}$ larger than diffusion time (i.e., at very small $\hat{t}$ diffusion plays a role) and for time small enough that the front of the advection $\hat{x}_f(\hat{t})$ is still between the two stagnation points, $\hat{\ell}/2 \le \hat{x}_f \le 1+\hat{\ell}/2$. For the initial condition, if we assume that the loading phase had a strong positive background flow (such as in the pressure-relaxation experiments), then surfactants have accumulated near the downstream stagnation point $\hat{x} = 1+\hat{\ell}/2$ for $\hat{t} \le 0$. The exact distribution of the surfactants at $\hat{t} = 0$ is unknown, but in the stagnant cap regime, we can assume that it is steep near $\hat{x} = 1+\hat{\ell}/2$. The constant of integration C is effectively a measure of the total amount of surfactant on the interface, which is constant at all times under our assumption of negligible exchanges with the bulk. This is effectively the main unknown in our experiments. We find

$$C = \left(\frac{\sqrt{3}}{2\sqrt{2}}\int_{\hat{x}_f}^{1+\hat{\ell}/2}\hat{\Gamma}\,\mathrm{d}\hat{x}\right)^{2/3}, \qquad \textbf{[S38]}$$

where $\hat{x}_f(\hat{t})$ is the front of the surfactant; i.e., where Γ vanishes,

$$\hat{x}_f = 1+\hat{\ell}/2-\sqrt{6C}\left(\hat{t}Ma\hat{H}\right)^{1/3}, \qquad \textbf{[S39]}$$

which is effectively valid in our finite-length geometry until the front reaches the stagnation point at $\hat{x} = \hat{\ell}/2$, as the model assumes a semi-infinite lane $\hat{x} \le 1+\hat{\ell}/2$. From [**S33**] and [**S37**], the interfacial speed due to surfactant gradients is therefore

$$\hat{u}_I = -\frac{1+\hat{\ell}/2-\hat{x}}{3\hat{t}}. \qquad \textbf{[S40]}$$

Thus, $\hat{u}_I$ is negative, corresponding to the backflow observed in our experiments (Fig. 4 *A* and *B*) for $\hat{t} > 0$. Once the loading phase ends and the background flow stops, the surfactants travel back along the interface, driving a Marangoni backflow, to eventually redistribute uniformly along the air–water interface, $\hat{\ell}/2 \le \hat{x} \le 1+\hat{\ell}/2$. This result also shows that the backflow velocity should decrease in time as $1/\hat{t}$. We compare this scaling prediction with our experimental results in Fig. 4*D*. As mentioned previously, this result is not valid at very small time, where diffusion processes and the unknown initial distribution of the surfactant have a strong influence on the Marangoni-driven flow. Hence, it cannot inform us about the dependence of the peak backflow velocity, measured at $\hat{t} \approx 0$, with U (Fig. 4*C*). It informs us only about the trend of the backflow at intermediate times, as shown in Fig. 4*D*, until the opposite stagnation point at $\hat{x} = \hat{\ell}/2$ starts playing a role. We also note that the interfacial velocity estimated in [**S40**] does not depend on the Marangoni number or on any other parameters. It depends only on the local gradient of the interfacial surfactant distribution, which depends on time and the spatial coordinate.

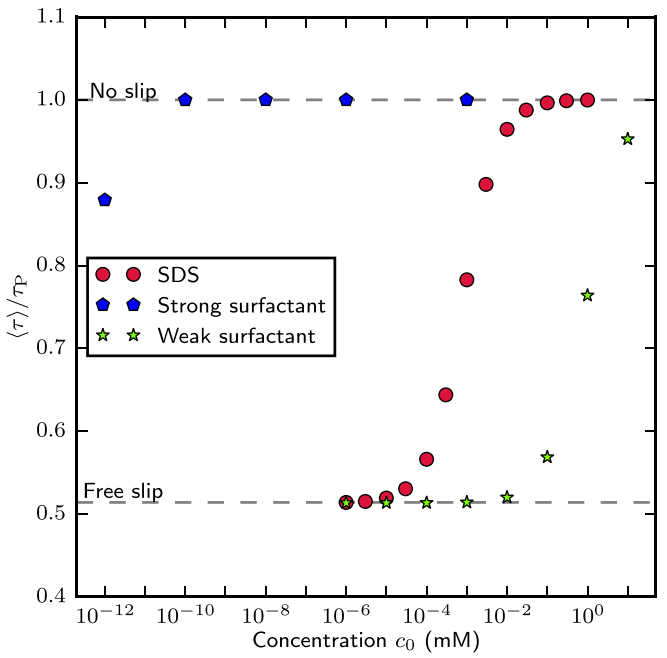

Fig. S1. Simulations of surfactant-laden flows in the 2D model SHS chamber shown in Fig. 2*A*. We compare the averaged normalized drag vs. the surfactant concentration for varying surfactant properties, using Frumkin kinetics. The SDS properties and the properties of the weak and strong model surfactants (defined using the extreme property values reported in ref. 40) are presented in Table S1. The associated characteristic nondimensional numbers of the SDS and the strong and weak model surfactants are presented in Table S2. The behavior of the transition is similar for all three surfactants, but it occurs at different concentration thresholds. The threshold is particularly low for the strong surfactant, $c_0 \le 10^{-10}$ mM.

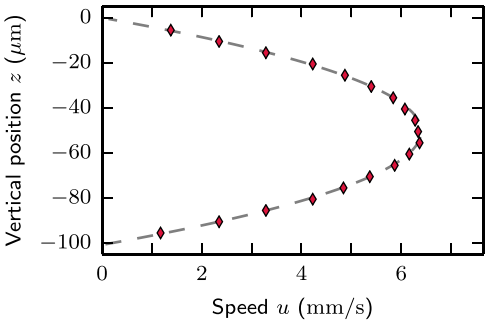

Fig. S2. Vertical distribution of the stream-wise velocity profile during the loading phase of the experiment presented in Fig. 4*A*. The dashed line shows the result of a parabolic fit of the velocity profile. The mean speed of the flow extracted from this fit is $U \approx 3.9\,\mathrm{mm{\cdot}s^{-1}}$.

Table S1. Parameters for 2D surfactant-laden simulations (Fig. 2 and Fig. S1)

Parameter	Symbol	Value	Unit	Use
Grating length	g	1×10^2	μm	Fig. 2 *B–D* and Fig. S1
		$20–10^4$	μm	Fig. 2*E*
Bulk concentration	c_0	1×10^{-6}	$\mathrm{mol{\cdot}m^{-3}}$	Fig. 2*B*
		1×10^{-2}	$\mathrm{mol{\cdot}m^{-3}}$	Fig. 2 *C* and *E*
		$10^{-6}–1$	$\mathrm{mol{\cdot}m^{-3}}$	Fig. 2*D*
		$10^{-12}–10^{-3}$	$\mathrm{mol{\cdot}m^{-3}}$	Fig. S1, strong surfactant (blue symbols)
		$10^{-6}–10$	$\mathrm{mol{\cdot}m^{-3}}$	Fig. S1, weak surfactant (green symbols)
Chamber height	H	1×10^2	μm	
Ridge length	ℓ	5×10^1	μm	
Maximum forcing speed	$u_{\max}$	5×10^1	$\mu\mathrm{m{\cdot}s^{-1}}$	
Mean forcing speed	U	3.3×10^1	$\mu\mathrm{m{\cdot}s^{-1}}$	
Water viscosity	μ	8.9×10^{-4}	$\mathrm{N{\cdot}s{\cdot}m^{-2}}$	
Water surface tension	σ_0	72×10^{-3}	$\mathrm{N{\cdot}m^{-1}}$	
Bulk diffusivity	D	7×10^{-10}	$\mathrm{m^2{\cdot}s^{-1}}$	Fig. 2 *B–E*
		1×10^{-11}	$\mathrm{m^2{\cdot}s^{-1}}$	Fig. S1, strong surfactant (blue symbols)
		1×10^{-9}	$\mathrm{m^2{\cdot}s^{-1}}$	Fig. S1, weak surfactant (green symbols)
Surface diffusivity	D_s	7×10^{-10}	$\mathrm{m^2{\cdot}s^{-1}}$	Fig. 2 *B–E*
		1×10^{-11}	$\mathrm{m^2{\cdot}s^{-1}}$	Fig. S1, strong surfactant (blue symbols)
		1×10^{-9}	$\mathrm{m^2{\cdot}s^{-1}}$	Fig. S1, weak surfactant (green symbols)
Desorption coefficient	κ_d	500	$\mathrm{s^{-1}}$	Fig. 2 *B–E*
		1	$\mathrm{s^{-1}}$	Fig. S1, strong surfactant (blue symbols)
		100	$\mathrm{s^{-1}}$	Fig. S1, weak surfactant (green symbols)
Adsorption coefficient	κ_a	89.5	$\mathrm{m^3{\cdot}mol^{-1}{\cdot}s^{-1}}$	Fig. 2 *B–E*
		1×10^6	$\mathrm{m^3{\cdot}mol^{-1}{\cdot}s^{-1}}$	Fig. S1, strong surfactant (blue symbols)
		1×10^{-1}	$\mathrm{m^3{\cdot}mol^{-1}{\cdot}s^{-1}}$	Fig. S1, weak surfactant (green symbols)
Maximum packing concentration	Γ_m	3.9×10^{-6}	$\mathrm{mol{\cdot}m^{-2}}$	Fig. 2 *B–E*
		1×10^{-5}	$\mathrm{mol{\cdot}m^{-2}}$	Fig. S1, strong surfactant (blue symbols)
		1×10^{-6}	$\mathrm{mol{\cdot}m^{-2}}$	Fig. S1, weak surfactant (green symbols)
Interaction coefficient	A	-2.4	—	Fig. 2 *B–E*
		-3	—	Fig. S1, strong surfactant (blue symbols)
		3	—	Fig. S1, weak surfactant (green symbols)
Surfactant style constant	n	2	—	

Table S2. Nondimensional parameters associated with Table S1 for 2D surfactant-laden simulations (Fig. 2 and Fig. S1)

Parameter	Fig. 2*B*	Fig. 2*C*	Fig. 2*D*	Fig. 2*E*	Fig. S1, strong surfactant	Fig. S1, weak surfactant
$Re = HU/\nu$	3.7×10^{-3}	3.7×10^{-3}	3.7×10^{-3}	3.7×10^{-3}	3.7×10^{-3}	3.7×10^{-3}
$Pe = gU/D$	4.7	4.7	4.7	0.9–470	330	3.3
$Pe_s = gU/D_s$	4.7	4.7	4.7	0.9–470	330	3.3
$k = \kappa_a c_0/\kappa_d$	1.8×10^{-7}	1.8×10^{-3}	1.8×10^{-7}–0.18	1.8×10^{-3}	10^{-6}–10^{3}	10^{-9}–10^{-2}
$Bi = g\kappa_d/U$	1.5×10^{3}	1.5×10^{3}	1.5×10^{3}	300–1.5×10^{5}	3	300
$\chi = g\kappa_d/(\kappa_a\Gamma_m)$	140	140	140	30–1.4×10^{4}	10^{-5}	10^{5}
$Ma = nRT\Gamma_m/(\mu U)$	6.6×10^{5}	6.6×10^{5}	6.6×10^{5}	6.6×10^{5}	1.7×10^{6}	1.7×10^{5}
$\hat{H} = H/g$	1	1	1	5–0.01	1	1
$\hat{\ell} = \ell/g$	0.5	0.5	0.5	2.5–5×10^{-3}	0.5	0.5
$\mathcal{D} = \chi(1+k)/Pe^{1/2}$	66	66	66–77	30–660	6×10^{-7}–5×10^{-4}	5.5×10^{4}–5.6×10^{4}
$\mathcal{K} = Bi(1+k)$	1.5×10^{3}	1.5×10^{3}	1.5×10^{3}–1.8×10^{3}	300–1.5×10^{5}	3–3×10^{3}	300†

†The variation of this parameter across the range of concentrations is not significant.

Table S3. Parameters for steady-forcing experiments (Fig. 3)

Parameter	Symbol	Value		Unit
		Fig. 3*D*	Fig. 3*E*	
Grating length	g	2	30	mm
Grating width	w	4×10^{1}	4×10^{1}	μm
Chamber height	H	1.3×10^{2}	1.0×10^{2}	μm
Ridge length	ℓ	2×10^{1}	2×10^{1}	μm
Ridge width	r	2×10^{1}	2×10^{1}	μm
Max. forcing speed	u_{max}	1.1×10^{2}	1.3×10^{2}	$\mu m \cdot s^{-1}$
Mean forcing speed	U	7.3×10^{1}	8.7×10^{1}	$\mu m \cdot s^{-1}$
Temperature	T	23	23	°C

Table S4. Nondimensional parameters associated with Table 4 for steady-forcing experiments (Fig. 3)

Parameter	Fig. 3*D*, assuming weak surfactant	Fig. 3*D*, assuming strong surfactant	Fig. 3*E*, assuming weak surfactant	Fig. 3*E*, assuming strong surfactant
$Re = HU/\nu$	0.01	0.01	9×10^{-3}	9×10^{-3}
$Pe = gU/D$	150	1.5×10^{4}	2.6×10^{3}	2.6×10^{5}
$Pe_s = gU/D_s$	150	1.5×10^{4}	2.6×10^{3}	2.6×10^{5}
$k = \kappa_a c_0/\kappa_d$	10^{-15}–10^{-3}	10^{-6}–10^{6}	10^{-15}–10^{-3}	10^{-6}–10^{6}
$Bi = g\kappa_d/U$	2.7×10^{3}	27	3.4×10^{4}	340
$\chi = g\kappa_d/(\kappa_a\Gamma_m)$	2×10^{6}	2×10^{-4}	3×10^{7}	3×10^{-3}
$Ma = nRT\Gamma_m/(\mu U)$	7.3×10^{4}	7.3×10^{5}	6.1×10^{4}	6.1×10^{5}
$\hat{H} = H/g$	6.5×10^{-2}	6.5×10^{-2}	3.3×10^{-3}	3.3×10^{-3}
$\hat{\ell} = \ell/g$	2.5×10^{-2}	2.5×10^{-2}	1.7×10^{-3}	1.7×10^{-3}
$\mathcal{D} = \chi(1+k)/Pe^{1/2}$	1.7×10^{5}†	1.7×10^{-6}–1.7	5.9×10^{5}†	5.9×10^{-6}–5.9
$\mathcal{K} = Bi(1+k)$	2.7×10^{3}†	27–2.7×10^{7}	3.4×10^{4}–3.5×10^{4}	340–3.4×10^{8}

Note that we assume the kinetics properties of the weak and strong surfactants described in Table 1, with a range of concentrations from $c_0 = 10^{-12}$ to 1 $mol \cdot m^{-3}$.
†The variation of this parameter across the range of concentrations is not significant.

Table S5. Parameters for 3D surfactant-free simulations (Fig. 3)

Parameter	Symbol	Value	Unit	Use
Bulk concentration	c_0	0	$mol \cdot m^{-3}$	
Grating length	g	2	mm	Fig. 3*D*
		30	mm	Fig. 3*E*
Grating width	w	4×10^{1}	μm	
Chamber height	H	1.3×10^{2}	μm	Fig. 3*D*
		1.0×10^{2}	μm	Fig. 3*E*
Ridge length	ℓ	2×10^{1}	μm	
Ridge width	r	2×10^{1}	μm	
Maximum forcing speed	u_{max}	1.2×10^{2}	$\mu m \cdot s^{-1}$	
Mean forcing speed	U	8×10^{1}	$\mu m \cdot s^{-1}$	
Water viscosity	μ	9.3×10^{-4}	$N \cdot s \cdot m^{-2}$	

Table S6. Experimental parameters of all of the pressure-relaxation experiments

Experiment	ΔH_r, mm	U, mm/s	Note
1-1	70	4.4	
1-2	−70	3.9	
1-3	70	4.3	
1-4	−70	3.9	
1-5	70	4.3	
1-6	−70	3.8	
1-7	70	4.3	
1-8	−70	3.8	
2-1	100	5.4	Adjacent grating failed
2-2	100	4.8	Adjacent grating failed
2-3	100	5.3	Adjacent grating failed
2-4	100	4.4	Adjacent grating failed
3-1	−40	2.3	
3-2	40	2.5	
3-3	−40	2.3	
3-4	40	2.5	
3-5	−40	2.3	
3-6	40	2.5	
3-7	−40	2.3	
3-8	40	2.4	Adjacent grating failed
3-9	−40	2.2	Adjacent grating failed
3-10	40	2.4	Adjacent grating failed
3-11	−40	2.2	Grating under study failed
3-12	40	2.5	Adjacent grating failed
4-1	130	7.4	Adjacent grating failed

Table S7. Nondimensional parameters for pressure-relaxation experiments in the loading phase (Fig. 4)

Parameter	$U = 2.3$ mm · s^{-1}, assuming weak surfactant	$U = 2.3$ mm · s^{-1}, assuming strong surfactant	$U = 4.1$ mm · s^{-1}, assuming weak surfactant	$U = 4.1$ mm · s^{-1}, assuming strong surfactant
$Re = HU/\nu$	0.25	0.25	0.44	0.44
$Pe = gU/D$	6.9×10^4	6.9×10^6	1.2×10^5	1.2×10^7
$Pe_s = gU/D_s$	6.9×10^4	6.9×10^6	1.2×10^5	1.2×10^7
$k = \kappa_a c_0/\kappa_d$	10^{-15}–10^{-3}	10^{-6}–10^6	10^{-15}–10^{-3}	10^{-6}–10^6
$Bi = g\kappa_d/U$	1.3×10^3	13	730	7
$\chi = g\kappa_d/(\kappa_a\Gamma_m)$	3×10^7	3×10^{-3}	3×10^7	3×10^{-3}
$Ma = nRT\Gamma_m/(\mu U)$	2.3×10^3	2.3×10^4	1.3×10^3	1.3×10^4
$\hat{H} = H/g$	3.3×10^{-3}	3.3×10^{-3}	3.3×10^{-3}	3.3×10^{-3}
$\hat{\ell} = \ell/g$	1.7×10^{-3}	1.7×10^{-3}	1.7×10^{-3}	1.7×10^{-3}
$\mathcal{D} = \chi(1+k)/Pe^{1/2}$	1.1×10^5†	1.1×10^{-6}–1.1	8.6×10^4†	8.6×10^{-7}–0.9
$\mathcal{K} = Bi(1+k)$	1.3×10^3†	13–1.3×10^7	730†	7.3–7.3×10^6

Note that we assume the kinetic properties of the weak and strong surfactants described in Table S1, with a range of concentrations from $c_0 = 10^{-12}$ to 1 mol·m^{-3}.

†The variation of this parameter across the range of concentrations is not significant.

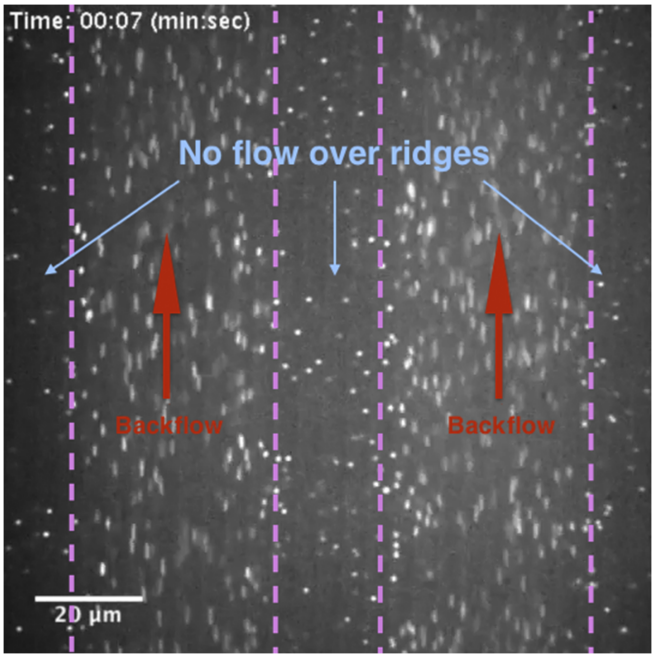

Movie S1. Flow over an SHS revealed by fluorescent microbeads in water imaged by spinning-disk confocal microscopy during a pressure-relaxation experiment. We record the flow ≈3 μm away from the plastron. The SHS consists of equispaced gratings, which are 30 mm long, 40 μm wide, separated by 20-μm wide ridges, and aligned with the flow direction (see Fig. 3 *A*–*C* and Tables S3, S4, and S6 for a detailed definition of the geometry and experimental parameters). The experiments begin with a loading phase, during which the flow (indicated by green arrows) is driven by a strong fixed pressure gradient and allowed to reach steady state (*SI Experimental Protocols* and Tables S6 and S7). The driving pressure is then rapidly decreased to zero while keeping the hydrostatic pressure approximately constant. A clear backflow, indicated by red arrows, in the direction opposite to the loading phase can be observed, thereby demonstrating the presence of Marangoni stresses.

Movie S1

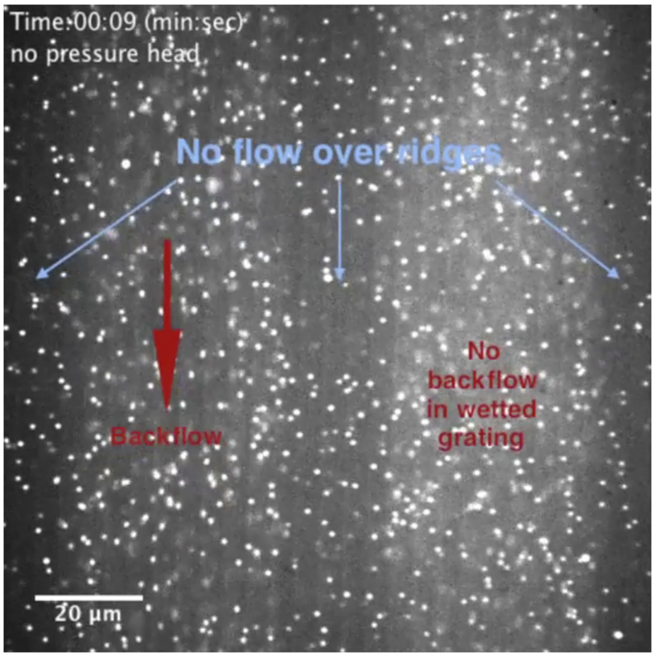

Movie S2. The flow over an SHS with conditions almost identical to those in Movie S1 (see Movie S1 legend for details), except that the right-hand side grating here is flooded, to contrast the different behavior observed when stopping the background pressure gradient. Similar to the flow above a ridge, the flow in the wetted grating stops immediately at the end of the loading phase, showing no backflow (this corresponds to experiments 2-4 in Table S6).

Movie S2